Faculty of Science and Technology
Department of Geosciences

Sedimentological and geochemical investigations of hydrothermally impacted sediments at the Aurora vent field, Fram Strait

Eivind Urbye Bjørnå

Master's thesis in Geology, GEO-3900, April 2023

Abstract

Hydrothermal vents are the result of the interaction between seawater and magma and occur at regular intervals along mid ocean ridges. The first visual confirmation of plumes was done in 1977. The detection of hydrothermal plumes has both provided indirect evidence for their existence and a resolution of the occurrences . In deep ocean with low sedimentation rates, hydrothermal plumites have the potential to become the dominant sediments.

The Aurora seamount (roughly 82.9° north and 6,2° west) sits at the western end of Gakkel Ridge, 166 km from the nearest landmass, with estimated annual seafloor spreading is around 14 mm per year. The presence of venting in water above the seamount was proven in 2001, and visual confirmation of the vent field was done in 2014. The samples analyzed in this study was gathered on and around the Aurora seamount with multi, blade, and gravity cores during the HACON cruises in 2019 and 2021. Shallow samples were the focus of stable carbon and nitrogen analyses, grain size analysis, quantitative XRF and XRD in order to describe the biogeochemistry and mineralogy on the vent field. Gravity cores distal to the vent field were described visually and scanned by Multi Sensor Core Logger in order to provide a basis for correlation between different lithologic units.

Findings in this study are the presence of rich deposits of iron and cupper sulfides in mounds on the rims of vents, responsible for providing sustenance to the chemolithoautotrophic communities. Only one sample from circa 1 m depth in a gravity core and 400 m south of the Aurora Vent Field was dated back to right before the Last Glacial Maxima (27123 to 27344 cal.yr. BP). However, it was not enough to accurately determine timing of different plumite layers. This study provides one estimate for annual average accumulation rates at the on the flanks of the Aurora seamount.

Acknowledgments

I feel lucky to have gotten the opportunity to be guided and supervised by Dr. Claudio Argentino (CAGE-UiT) as well as Professor Giuliana Panieri (CAGE-UiT) and I want to thank them for the gift of knowledge.
I want to praise all the amazing work that was done on the HACON 19 and 21, that have provided me access to a depth of data from an alien environment, and hopefully let me contribute with a little piece of the puzzle. This would not have been possible without the NFR-funded AKMA and HACON projects for the material and funding supporting the analytical methods.
I am very grateful for the work of Dr. Pierre-Antoine Dessandier (IFREMER), for all the thorough analysis of samples.
Thanks to the beautiful blade core picture provided by Dr. Sofia Ramalho (UA).
Thank you, Geo Lab staff: Trine Dahl, Ingvild Hald, Karina Monsen, and Johan Matteus Lindgren for the work you have done on the analysis hand help I received on the lab.

Lastly, I want to dedicate a special heartfelt thanks to my fiancée Vilde for all the love and support (as well as Luna, our dog, for comic reliefs).

Eivind Urbye Bjørnå

May 2023

Table of Contents

1 Hydrothermal vents 1
1.1 Global distribution 1
1.2 General sub seafloor dynamics 3
1.3 Hydrothermal plumes and oceanic metal contributions 4
2 Biogeochemistry of hydrothermal sediments 5
2.1 Microbial ecology 5
2.2 Macrofauna community 5
3 Study area: Aurora Vent Field, Fram Strait 6
3.1 Geological setting 6
3.2 Aurora 8
4 Data and methods 9
4.1 Sediment coring 9
4.1.1 ROV samplings 10
4.1.2 Gravity coring 10
4.1.3 Multicoring 10
4.1.4 Pore fluid analysis 11
4.2 Nondestructive core scans 12
4.2.1 Multisensor core logging 12
4.2.2 X-ray Fluorescence 12
4.3 Core Visual Description 13
4.4 Major and trace element analysis 13
4.4.1 Xray fluorescence (XRD) analysis 13
4.4.2 Xray Diffraction (XRD) analysis 14
4.5 Carbon-nitrogen geochemistry (TOC, TN, δ13C & δ15N) 14

4.6 Grain Size Analysis 15
4.7 Radiocarbon Dating of Planktonic Foraminifera 15
5 Results 17
5.1 Core lithostratigraphy 17
5.2 Core geochemistry and mineralogy 29
5.2.1 XRF 30
5.2.2 XRD 35
5.2.3 Stable Isotope Analysis 37
5.3 Pore fluid geochemistry 39
5.4 Sediment core correlation 41
6 Discussion 42
6.1 Sediment biogeochemistry 42
6.2 Origin of hydrothermal sediments 43
6.3 History of vent activity on Aurora Seamount 45
7 Conclusions 48
References 50

1 Hydrothermal vents

The first observation of deep submarine hydrothermal vents was done at the Galapagos Rift in the Pacific Ocean in 1977 (Beaulieu et al. 2015), this discovery was an essential component of the continental drift theory that started to gain traction in the scientific community only decades before this. Alfred Wegener hypothesized there once existed a super continent from the way some adjacent coastlines seemed to have some degree of inverse shape to one another (Nystuen, 2007, p. 24). Wegener's problem was how to explain how continents could drift apart, but bathymetric mapping in the 50s and 60s changed that. The ocean floor was revealed to have wide range of features ranging from vast abyssal plains, lone seamounts, deep trenches, and extensive underwater mountain ranges. These submarine mountain ranges happened to be placed in the middle of oceans between several of the coastlines with matching contours, giving them the name mid ocean ridges (MOR). With the discovery that magmatic rocks below the ocean floor increased continuously in age the further away from the MORs and towards continents and submarine trenches, there was no doubt that the MORs was an axis of volcanism creating new seafloor (Nystuen, 2007).

As one might expect there is huge temperature difference between liquid rock and deep ocean seawater, giving magma plenty of opportunity to be cooled before it can reach the surface, this will be enforced if there is a high porosity or large concentration of cracks surrounding ascending magma. The water that makes it down will heat up to 350 to 400° C causing the fluid to rise, dissolve and react with the mafic rock (McCollum & Shock, 1997). The points in the surface where these fluids escape is known as hydrothermal vents, and collections of vents are called vent fields, of which some vents may be inactive or completely extinct.

1.1 Global distribution

The MORs are the most extensive volcanic systems on Earth, with this style of volcanism being responsible for the creation of nearly all oceanic crust the last couple of hundred million years. Back-arc spreading centers also experience limited volcanism due to rifting, but globally such axis constitutes 6 times less length than the MOR (Beaulieu et al., 2015).

241 vent fields have so far been located worldwide at depths exceeding 200 m (Beaulieu, 2016). A vast majority of vents are located on the mid ocean ridges, Beaulieu et al. (2015) suggests around 900 vent fields remain to be discovered based on the frequency of vent fields mapped or detected along mid ocean ridges. Hydrothermal vents are not exclusive to MOR systems and are known to occur over mantle plume hotspots. Among the vent fields on MORs differences can be drawn from the rate of spreading, this can vary from almost no annual movement to 170 mm per year, the rates can be divided into five different rates as described in the description of *Figure 1*. Previously there was assumed to be a roughly linear relationship between the rate of spreading and the frequency of vents found along the axis of MORs, this prediction is not very accurate when compared to the MORs surveyed so far. The frequency of vents seems to plateau when the spreading rate is fast and ultra-fast (>80mm/yr) varying with a vent field for every 25 to 30 km, while there is little change in frequency of ultra-slow and slow spreading ridges(0-55mm/yr) with vent fields locations approximately every 100 km (Beaulieu et al., 2015). The Piccard vent site is located on the ultra-slow spreading Mid Cayman Rise at a depth of 5000 m +-50 m. This is the deepest detected hydrothermal vent by the time of this publication, beating the previous record for deepest confirmed vent Ashadze 13°N in the Mid Atlantic Ridge by approximately 800 m (German et al. 2010).

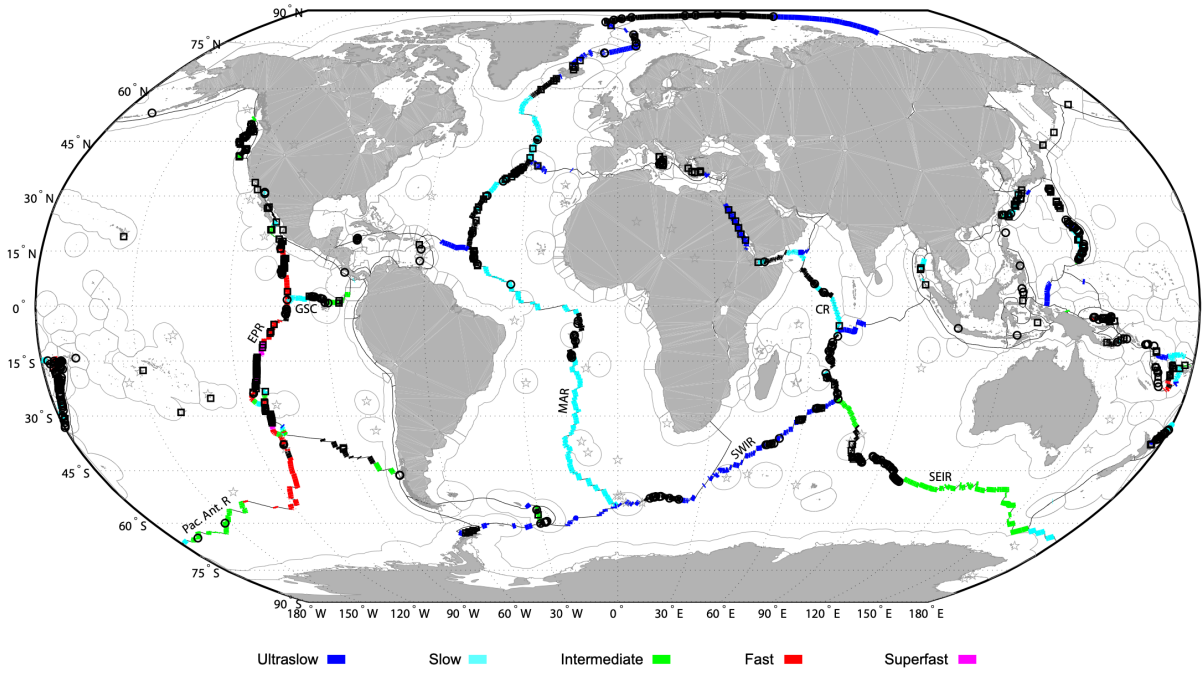

Figure 1. by Beaulieu et al. (2015) Global map of mid ocean ridges with the different rates of spreading ultraslow (0-20 mm/yr), slow (20-55 mm/yr), intermediate (55-80 mm/yr), fast (80-140 mm/yr), and superfast (>140 mm/yr). The black squares are vent fields discovered before the turn of the millennia, black dots are vent fields discovered after and open stars are mantle plume hotspots.

1.2 General sub seafloor dynamics

The fluids ejected from vents are assumed to be originally from local seawater diffusing into sediments and faults, although considerable amounts of water do exist in the mantle (Yoshino, & Katsura, 2013) it would be unlikely that it represents a substantial source of fluids to hydrothermal vents beneath the oceans.

Sulfate is the second most abundant anion in seawater (Klotz et al., 2011) and will thus be present in sediment porewater in substantial quantities when not consumed. Above 38°C in anoxic conditions when there is enough H_2 the conditions become favorable for reduction of sulfate, see *Formula 1*. This reaction can be utilized as source of energy for anaerobic microorganisms, but the free energy yield is still several hundred times smaller per mol than that yielded by the oxidation of H_2S (McCollum & Shock, 1997).

$$SO_4^{2-} + 2H^+ + 4H_2(aq) = H_2S(aq) + 4H_2O \quad (Formula\ 1)$$

$$2FeO + H_2O = Fe_2O_3 + H_2 \quad (Formula\ 2)$$

$$\sum CO_2 + 4H_2 = CH_4 + 2H_2O \ (Formula\ 3)$$

Through the process described in *Formula 1* large deposits of sulfides can continuously build up around where the fluids escape the surface and meet the contrasting cold sea water precipitating with cations and in many cases creating walls akin to chimneys. During serpentinization of mafic rocks, the ferrous iron in olivine will be oxidated by oxygen from water molecules, converting fluid inclusions from water to hydrogen, the generalized reaction in *Formula 2* can continue until all water is converted, with optimal temperature being around 300°C (Klein, Grozeva, & Seewald, 2019). Hydrogen production will be most intense at hydrothermal vents where water is continuously circulating into contact with olivine from cooling magma. Any carbon present in the fluid can generate methane through the reaction in *Formula 3* and provide water back to the production of more hydrogen in *Formula 2* (Klein, Grozeva, & Seewald, 2019).

The temperature of the venting fluids correlates to differences in deposits at the sites. 250°C causes talc and anhydrite formation, 270°C typically observed as white smokers causes sulfide, sulphate, iron oxide-hydroxide to form, while 320°C seen as black smokers leave mounds of sulfide (Pedersen et al., 2010).

1.3 Hydrothermal plumes and oceanic metal contributions

Hydrothermal plumes are beyond doubt major parts of the cycling of elements between the ocean and the Earth's crust, moreover the plumes can act as pumps of essential limiting nutrients into the photic zone. Of the Earth's oceans 40 % have dissolved iron as the limiting nutrient for primary production, while vents can increase the concentration with a millionfold compared to the levels of the surrounding seawater (German et al., 2016).

Hot vent plumes can travel hundreds of meters in the water column before it reaches zero buoyancy and cools to become as dense as the surrounding seawater. It is assumed that the plumes spread out in an up-side-down cone shape with a maximum angle of 30° up from the vent (German et al.2010). The positive temperature anomaly produced by plumes are in the order of a hundredth of a Celsius degree one km above the vents (Stranne et al., 2010) and ejected hydrothermal fluids quickly become diluted by seawater by a factor of around 10000:1 within the plumes (German et al., 2016).

2 Biogeochemistry of hydrothermal sediments

Hydrothermal vents are habitats that seem alien and inhospitable to us humans, but in the frame of reference to the organisms calling this home, it is terrestrial life that has evolved the most distant form compared to the last universal common ancestor (Weiss et al., 2016).

2.1 Microbial ecology

Beneath the oceans photic zone, the most available source of energy for microbes will be the marine snow and other dissolved organic matter (DOM), where very little of the marine snow make it down to the deepest depths. Hydrothermal vents stand out as oasis for life in contrast to the meager surroundings of the deep sea, rather than acquiring energy from absorptions of light in photosynthesis the primary producers in these communities are chemoautotrophic, meaning these organisms grow and expend energy that is available from the reductive potential of compounds emitted by hydrothermal vents (McCollum & Shock, 1997). Hydrothermal vents release several elements and compounds in various concentrations that can be used as electron donors, of which H_2S and FeS and Fe(II) are the most important, with H_2 and FeS_2 forming in the plume (Lengeler et al., p. 773). Microbial communities inside the plumes are crucial in our understanding of ocean biogeochemistry (Molari et al., 2022). Due to the intense mixing with cold oxygenated seawater, the plume provides more favorable conditions for oxidation of CH_4 H_2 H_2S (McCollom & Shock, 1997), but also many other elements such as ferrous iron. Molari et al., (2022) found from the plume of the Aurora seamount a species they named *sulfurimonas pluma,* had adapted to tolerate O_2 better than contemporary known species of *Sulfurimonas* that usually are found in redoxcline of sediments.

2.2 Macrofauna community

Several invertebrate species have evolved adaptations to thrive near hydrothermal vents. As the entire food web is so concentrated it is a perfect environment for sessile animals, such as bivalves, tube worms, cnidarians, and sponges to specialize, many of which have developed symbiotic relationships with chemoautotrophic prokaryotes (Lengeler et al., p. 774). Benthic animals can graze on bacterial mats, while species that are not themselves endemic to the vents can feed higher up on the food web.

3 Study area: Aurora Vent Field, Fram Strait

The Aurora seamount is in the Fram Strait, Arctic Ocean roughly 82.9° north and 6,2° west. The closest landmass is Princess Ingeborg Peninsula, northwestern Greenland 166 km southwest of the site, to the southeast the closest land is Northwestern Spitsbergen roughly 440 km away.

3.1 Geological setting

The Gakkel Ridge is the MOR of the Arctic Ocean oriented in a line 1800 km long the on the eastern flank of Earths North Pole, bringing the middle section at approximately 60° east the farthest north at 87°. The Aurora seamount is situated at the western termination of the Gakkel Ridge where the MOR makes an approximately 40° bend from north-northeast to south that connects Gakkel to the Lena Trough in the North Atlantic (*Figure 2*). The eastern termination of the Gakkel Ridge is in the Laptev Sea at approximately 81° north and 120° east, where it lies in connection to the plate boundary between the Eurasian and North American plates across Siberia (Michael et al., 2003). The spreading rate at the Gakkel Ridge can be characterized as ultra-slow through its entirety, with the slowest occurring on the part of the ridge between 3° and 29° east, while between 37° and 43° east the rate is 12.7mm and 11.0mm per year respectively (Michael et al., 2003). The fastest spreading rate of the Gakkel Ridge occur in the western part of the ridge where spreading rate is 13.5 and 14.5 mm/yr (Michael et al., 2003).

Of all major MORs, the Gakkel Ridge has the deepest average depth, but the Western portion is shallower than the central and eastern (Michael et al., 2003). The Rift valley of the Northern part of the Lena Trough reach a depth of 4800 m several places between 5 and 50 km south of the Aurora seamount summit, while the rift valley floor of the Gakkel ridge northeast of Aurora varies between 3300 m and 4400 m depth (see *Figure 2*).

The rift valley floor surrounding the Aurora seamount has more than 90 % of the seafloor covered in muddy gray clays, with a typical thickness of 3.5-5-5 m (German et al. 2022), this was also an observation on the HACON-19 cruise, with only one recovered core believed to consist of coarse-grained ice rafted debris (Bunz & Ramirez-Llodra, 2019). Beneath the thin sediments the crust would be largely mafic, the AMORE 2001 recovered pillow basalts even on the axial valley walls, no peridotites were dredged from the western portion of the Gakkel Ridge (Michael et al., 2003). In the continuation of the Arctic Mid Ocean Ridge (AMOR) between the Fram Strait and Iceland, that Gakkel is part of there are several examples of thick packs of continentally derived sediments interjecting with the spreading axis (Pedersen et al., 2010).

The passive margins on each side of the western region of the Gakkel ridge is flanked by Morris Jesup Rise north of Greenland and the Yermak Plateau north of Svalbard. These two plateaus are believed to have been connected as one before the rifting occurred sometime before the Oligocene 33 million years (Ma yr.) ago (Lasabuda et al., 2021), with ocean filling the rift valley in the Miocene from 15 – 20 Ma yr. ago (Engen et al., 2008). The process of this opening of the Fram Strait is still ongoing, as evidenced by the rift valley walls of inward stepping normal faults. The axial hills and normal faults of the western Gakkel ridge are relatively straight, with little or no ridge offsets and transverse faulting to speak of (Michael et al., 2003). The present mode of seafloor spreading in the Fram Strait has occurred since around 10 Ma yr. ago (Engen et al., 2008).

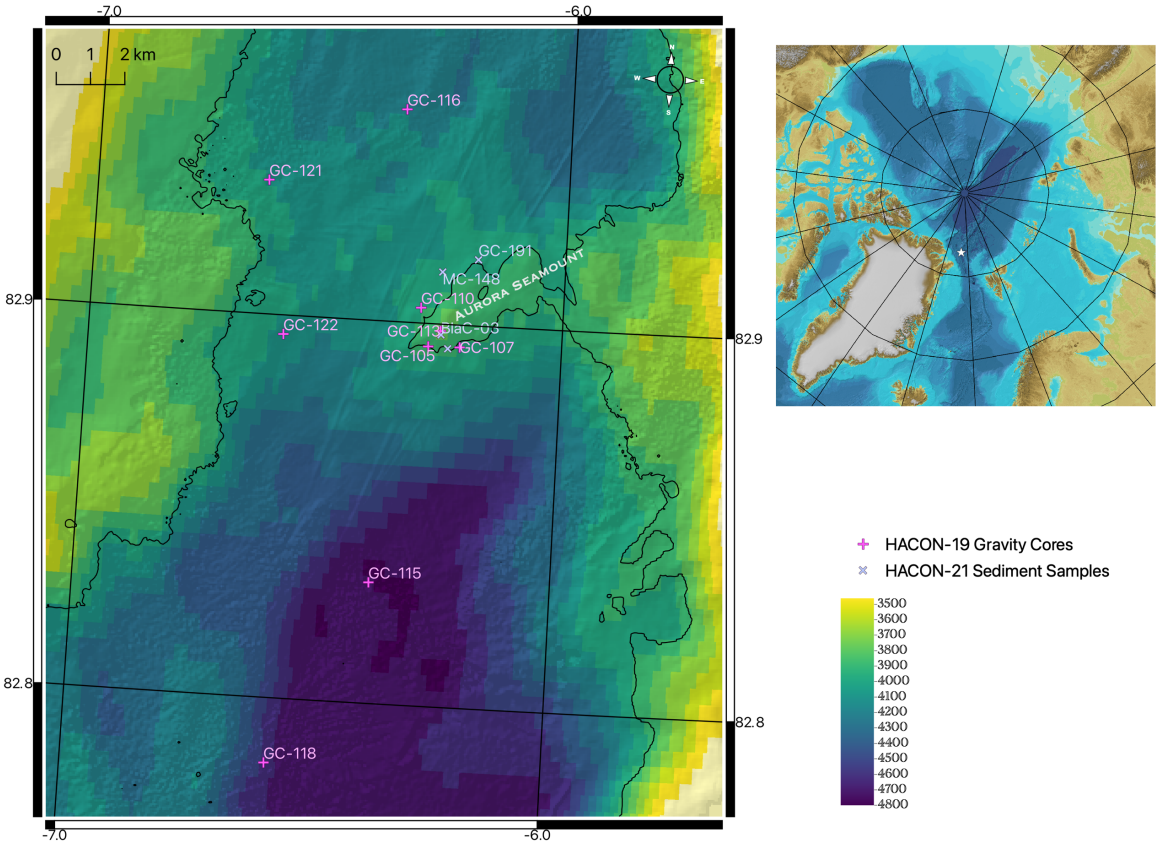

Figure 2. Bathymetry of the study area, with the locations of sediment cores on and in proximity to the Aurora Seamount. From HACON 19 cruise, we only report the gravity cores, whreas for HAON21 we reported the location of gravity cores (GC), multicores (MC) and Blade cores (BlaC). Blade cores are less than 5 m from each other so they overlap at this scale. Gravity core GC-124 [81°42'41.8"N; 6°11'43.5"W] is not shown in this map because it is located far off the Aurora vent field, 119 km south of GC-118. The color palette is accessible to people with color vision deficiencies. Overview map top right is of IBCAO 400x400 (Jakobsson et al., 2012).

3.2 Aurora

The Aurora seamount is located on the Rift valley floor of the Arctic Mid Ocean Ridge at the junction between the Lena Trough to the south and sits within the southwestern end of the Gakkel Ridge (*Figure 2*). Its summit at roughly 3840 m depth, stands 1000 m above the lowest parts of the valley floor to the south but is merely 300 to 400 m higher than the rift valley floor to its northeast. Aurora is itself one of five axial volcanic ridges between 6° west and 3° on the Gakkel Ridge (Michael et al., 2003). Of the registered active vents, two have been named as of the HACON-21 cruise, Hans Tore and Enceladus, while the third was named Ganymede later (Ramirez-Llodra et al., 2023), located half a km south of the Aurora summit. Hans Tore was named in honor of the late deep sea marine biologist Hans Tore Rapp, that was pivotal in the HACON project, while Enceladus is named after the ice-moon

orbiting Saturn (Bunz & Ramirez-Llodra, 2021), while Ganymede is a Jupiter moon, the biggest in the Solar system is also thought to host liquid water (Ramirez-Llodra et al., 2023). The inactive chimneys that have been mapped on the seamount are in an elongate cluster with the length somewhat parallel to orientation of the Gakkel Ridge. Since the first discovery of deep-sea hydrothermal vents, it has been suggested that slow spreading mid ocean ridges could host hydrothermal vent systems (Beaulieu et al., 2015), the first proof of this over this part of the Gakkel Ridge was made in during the AMORE 2001 cruise (Michael et al., 2003). The Aurora seamount first got its name from the 2014 PS86 AURORA expedition in 2014 when the first observations of venting were made with the ship towed Ocean Floor Observation System. The next expedition was the HACON-19 cruise, with several different coring techniques successfully retrieving samples and more thorough visual data being collected by Nereid Under Ice (NUI) vehicle (Woods Hole Oceanographic Institution, USA) (Ramirez-Llodra, et al. 2023). The most recent cruise (HACON-21) was the first time a ROV was able to take samples and high-resolution seafloor imagery from the Aurora Vent Field (AVF) (Bunz & Ramirez-Llodra, 2021). The reason for advances of this part of the global ridge system being so incremental are due to the extra challenges that present themselves on top of the difficulties that is associated with deep sea research. The entirety of the Gakkel ridge is beneath an ocean that is partly frozen during large parts of the year, this requires equipment that is extra tough and good knowledge of the condition that can be expected.

4 Data and methods

This section presents the methods that has been applied to produce the results of this thesis and summarizes the mechanisms and technical aspects.

4.1 Sediment coring

Both HACON cruises took place during the autumn as this is the time of year when the ice cover is at its weakest, being reduced to ice floes with enough sea surface to conduct underwater operations with unmanned vessels. Sediment cores were collected via gravity coring (GC), multicoring (MC), and ROV-guided blade (BC) and push coring (PC).

4.1.1 ROV samplings

Dive paths of the ROV were planned in advance and ice floe movement below 0.3 knots were deemed as the optimal conditions for this (Bunz & Ramirez-Llodra, 2021). During the drifting of the ship the ROV would descend at a speed of 0.8 m/s, when the ROV reached the target area it would be maneuvered around with its 7 thrusters (Bunz & Ramirez-Llodra, 2021).

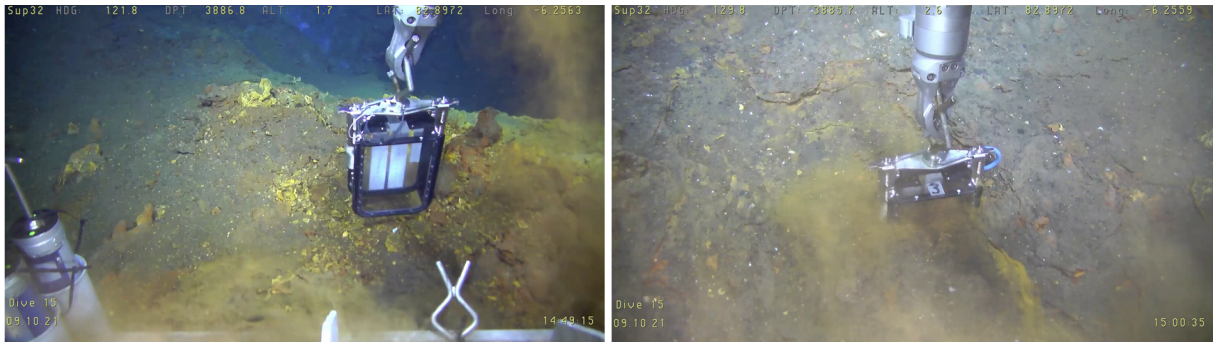

Figure 3. Video stills capturing the moment before BlaC01 is thrust into the sediments on the left, and the on the right BlaC03 has penetrated into the seabed.

The blade cores are picked up from a compartment on the ROV by its manipulator arm and pushed into the seabed of interest (see *Figure 3*). Blade cores can reach a maximum depth of 32 cm below sea floor (bsf), has a thickness of 10 cm and a width of 25 cm (Bunz & Ramirez-Llodra, 2021). Push corers are likewise pushed into a desired point of seabed, but its dimensions are a 56 cm long cylinder with an inner diameter of 8 cm (Bunz & Ramirez-Llodra, 2021).

4.1.2 Gravity coring

Gravity coring were performed with a 6 m long steel cylinder of 11 cm outer diameter with a PVC liner of 10 cm inner diameter placed inside the steel cylinder. At the end of the gravity core a core catcher and core cutter is placed in order to penetrate deeper into the sediments while retaining as much material as possible. Iron weights on the top of the core provide extra mass. Once in the water the gravity core is lowered at a speed of 1 m/s, until the last 50 m above the seabed when the entire 1,3-ton contraption is released to accelerate towards the seabed with the power of gravity (Bunz & Ramirez-Llodra, 2019).

4.1.3 Multicoring

The multi corer (MC) consist of 4 70cm transparent plastic liners with a diameter of 10cm held in place by the KC Denmark DK8000. During operation the set is lowered towards the

seafloor at a speed of 1 m/s, the last 50 m to the seafloor the speed is reduced to 0,5 m/s. Once it reaches the seafloor 1 minute is provided for it to settle with the lead weights on top providing the force to push the liners into the sediment. The contraption is lifted back to the ship at a speed of 1 m/s (Bunz & Ramirez-Llodra, 2021).

Figure 4. KC Denmark DK8000 on the ship deck after a successfully retrieving MC-148. 1. Plastic liners in the MC, 2. lead weights to provide gravitational force into the sediments, 3. core catchers to retain sediment upon retrieval. Edited after (Bunz & Ramirez-Llodra, 2021).

4.1.4 Pore fluid analysis

Syringes with volumes of roughly 5 mL were filled with sediment extracted from the gravity cores and blade cores and injected into 20mL serum vials containing 5 mL of 1M NaOH, these vials were then immediately thoroughly sealed, shaken, and placed upside down in order to equilibrate (Bunz & Ramirez-Llodra, 2021). Vials were stored at 4°C until the headspace gas were measured in a ThermoScientific GC Trace 1310 gas chromatograph-mass spectrometer at the Stable Isotope Laboratory at CAGE— Centre for Arctic Gas Hydrate, Environment and Climate, located at UiT—The Arctic University of Norway in Tromsø, Norway.

Blade core and multicores had holes predrilled for pore water analysis, in which Rhizon tubes 5 cm long, and prewetted in MilliQ water for at least 30 minutes prior, were inserted. 10 mL plastic syringes extracted pore fluid with the negative pressure generated by pulling the spacers back. Finally, the aliquots for measuring Dissolved Inorganic Carbon (DIC) were

taken, these consisted of less than 1 mL of sample, 10 µL $HgCl_2$ was added to stop microbial activity, and stored at 4ºC (Bunz & Ramirez-Llodra, 2021).

4.2 Nondestructive core scans

4.2.1 Multisensor core logging

The same instrument used in the nondestructive XRF scan also possesses the ability to exert an external magnetic field and gauge the sediments magnetic response to this, giving the results in 10^{-5} susceptibility index.

High resolution images were taken of every section of the gravity cores by the Geotek Multi-Sensor Core Logger (MSCL) (Geotek Ltd., n.d.). X-ray images were also produced with the exposures revealing most detail being selected by a lab operator. The parts of the core that are denser should absorb more X-rays, representing the darker layers (Smith et al., 2020).

Fractional Porosity (FP) values are calculated from the attenuated gamma density, as long as some assumptions can be made for the material in the core, such as the pore spaces being fully saturated in water, and the average grain size density (Geotek ltd., 2016). Attenuated Gamma density values are produced by measuring the gamma rays from a radioactive source, usually ^{137}Cs, that make it through the core, less gamma rays imply a higher density due to more attenuation(loss) (Ross & Bourke, 2017)

4.2.2 X-ray Fluorescence

This method was applied to the gravity cores 191 and 193. The method works by exposing the sample surface to x-rays, this radiation will cause atoms to be excited, and fluorescent rays emitted when electrons return to their initial energy state in the atom. The secondary radiation is registered by the scanner and the signals converted to counts that correspond to the respective elements. The Avaatech XRF core scanner has an X-ray with a rhodium anode that produces X-rays frequency depending on the voltage applied to the cathode. The scanner that detects the secondary radiation registers element numbers from 12 (Mg) to 92 (U), with higher voltage needing to be applied to detection of heavier elements (Forwick, 2013). The core was scanned at 10 kV with 1000 µA for elements between Mg and Co, 30kV with 2000 µA for elements between Ni and circa Mo, and lastly 50 kV with 2000 µA for elements heavier than Mo. Filters needs to be applied to the scanner when measuring at 30 and 50 kV,

palladium thick filter and a copper filter respectively (Forwick, 2013). The reasoning for this is to remove noise from lighter elements when measuring secondary radiation at higher voltage, this voltage dependent variance in measurement mean that the data are not quantitative, but rather semiquantitative, yielding relative variations of elements in the core and providing a mean to demonstrate the presence of specific elements. During the measurement, the core surface is covered with a foil transparent to X-rays with a helium filled chamber between this and the scanner so that the interaction between X-rays and atmospheric air is not interfering with the results (AvaaTech, n.d.).

4.3 Core Visual Description

The PVC lining of the gravity cores were sawed across their length and carefully split open. A plastic card was used to scrape the split surfaces parallel with inclined layers so that as little crossing of particles between neighboring layers could occur. One of the halves were carefully tucked plastic foil and sealed into plastic before being sent to the archive.
When comparing the exposed facies with a Munsell Color Chart (Pendleton & Nickerson, 1951), the core was placed near a window in the lab so it could be inspected in daylight, to observe a wider and more balanced range of colors in the cores. All visible structures, and apparent changes in grain size were also noted.

4.4 Major and trace element analysis

A selection of samples was collected from intervals of the aforementioned gravity cores based on peaks in magnetic susceptibility or peaks in XRF signals from elements that are indicative of hydrothermal input, such as Fe. Blade cores, and multi core, these were then oven dried overnight at 40°C in order to be shipped to the laboratory of Ifremer (Brest, France)..

4.4.1 Xray fluorescence (XRD) analysis

X-ray diffraction (XRD) analyses were conducted with a BRUKER AXS D8 Advance diffractometer hosted at Ifremer (Brest, France). 17 samples were top loaded into 2.5 cm diameter circular cavity holders, and all analyses were run between 5° and 70° 2θ, with 0.01° 2θ step at 1s/step (monochromatic Cu Kα radiation, 40 kV, 30mA). Minerals were identified using the Diffrac.Suite EVA software. This methodology allows to quickly identify most

minerals (e.g., silicates, carbonates, well-crystallised manganates, well-crystallised iron oxyhydroxides) (P.A. Dessandier, personal communications, March 2023).

4.4.2 Xray Diffraction (XRD) analysis

X-ray fluorescence analyses were conducted at Ifremer (Brest, France) with a wavelength dispersive X-ray fluorescence spectrometer (WD-XRF; BRUKER AXS S8 TIGER) on fusion beads or compressed pellets (for major and trace elements, respectively). After data acquisition, measured net peak intensities corrected from inter-element interferences were converted into concentrations using calibration curves generated from the analysis of certified reference material powders, measured under identical analytical conditions (P.A. Dessandier, personal communications, March 2023).

4.5 Carbon-nitrogen geochemistry (TOC, TN, δ13C & δ15N)

The carbon-nitrogen geochemistry (TOC, TN, $\delta^{13}C$ & $\delta^{15}N$) of sediment cores was investigated to provide information about microbial productivity from chemosynthesis and the predominant mode of metabolism (Whiticar, 1999; Won et al., 2018) at different levels of the near surface sediment of the hydrothermal vent field. In preparation for this method the 62 samples, of which 6 were replicates, needed to be crushed with 6mm retsch steel balls inside the tubes on a shaking table at 15 Hz, 10 minutes was enough for the samples from the BlaCs, while the reference MC-148 was shaken twice the time because the clumps were more resilient. The retsch balls were cleaned with lint free paper, ethanol, and distilled water between uses. The crushed samples were soaked in 6 M HCl for over 48 hours in room temperature to remove carbonate. The samples were washed with distilled water to remove excessive acid, before being dried at 50°C.

At this stage of the pretreatment of the samples, the aliquot taken need to be constrained precisely and kept in a container that also can be combusted with it. Tiny tin (Sn) capsules are used as containers, these may have small variations in weight, so the weighing instrument needed to be reset between each new Sn capsule being used.

Combustion happened in EA (Thermo Scientific Flash HT Plus) at 1020C and is analyzed on IRMS (Thermo Scientific MAT253) hosted at the Stable Isotope Lab-SIL (Department of Geosciences, UiT).

4.6 Grain Size Analysis

The hydrothermal environment contains some extreme transitions between hot and cold, and reducing and oxidizing conditions respectively (McCollom & Shock, 1997). As the flux from the vents tend not to change drastically over short time, it provides an environment that can be colonized by chemoautotrophic thermophile microbes along the transitions certain species are best suited for. Pore space in this critical transition can play a crucial role on the mixing that occur between seawater and hydrothermal fluids, with a higher proportion of small grains limiting diffusion, making the temperature and chemical gradient steeper. This method measures the mean grain sizes of samples after organic and carbonate particles are removed. Between 1.90 and 2.00 g from each interval has 20% HCl added until all of it is soaked in the acid, 5 samples from each the upper 5 cm the multicore and two blade cores, 15 in total, were left in this step for over 24 hours. Next step was to remove the acid by repeated dilution. In order not to lose any grains from the test tubes, they were placed in a centrifuge for 4 minutes at 4000 round per minute. After the third time the sample were sufficiently neutral to soak it in 20% H_2O_2. To catalyze the oxidation of organic compounds, the test tubes were heated by a warm bath at 85°C for two hours. The tubes were lifted from the warm bath if reactions were too violent, and aluminum foil covered the tops to limit spraying and make the work safer. When diluting away H_2O_2 from the samples the same procedure was taken as when diluting HCl. When the samples were sufficiently neutral again, they were moved into plastic tubes and dried to weigh the remaining constituents of the samples.

Because the remaining fraction of the samples ranged between 0.17 and 0.45 g, all of it was used in the next steps. Around 20 mL of distilled water is added with the samples in a beaker and placed on a shaking table for over 24 hours. To inhibit clumping during measurement of grain sizes one to two drops of Calgon soap-solution was added in the beakers. Lastly each sample was run three times through the Beckman Coulter LS 13 320 Particle Size Analyzer in the GeoLab (Department of Geosciences, UiT).

4.7 Radiocarbon Dating of Planktonic Foraminifera

This method is used to measure the apparent time that has passed since an organism lived meaning the period it incorporated carbon from its environment. Carbon14 (^{14}C) is created in the atmosphere when the most common isotope of nitrogen(^{14}N) captures a neutron from

cosmic radiation in its nucleus and ejects a proton resulting in it changing to the radioactive isotope ^{14}C (Korrf, 1940) with a half-life of about 5600 years (Libby, 1960). Because this process occurs at Earth's surface, this causes atmospheric carbon to be the single most important pool for ^{14}C at any time on Earth. As there is a much larger pool of inorganic carbon in the ocean than in the atmosphere, it is the organism that consume organic material made by autotrophy in the surface that incorporate ^{14}C into their bodies. Thus, the proportion of ^{14}C to ^{12}C that is measured in organisms consuming chemoautotrophic biomatter would greatly exaggerate the age since the organism was alive. Therefore, only organisms assumed to have lived in the photic zone near the ocean surface are considered for carbon dating in this study. Foraminifera are a diverse class of protozoa have many known species with carbonate tests that vary in shape from species to species, with planktonic species such as *globigerina pachyderma (sinistral)* typical for the polar regions (Armstrong, 2004, p.158).

Six sediment intervals, three on each of the core's GC-191 and GC-193 were chosen for picking of planktonic foraminifera tests to be carbon dated. Those intervals were selected based on high values of Ca/Ti in the XRF scans which suggested sufficient amounts of foraminifera for radiocarbon dating. The chosen sites were then carefully collected, taking care not to collect to close to the PVC liner where sediments from other layers in the sediment could be sheared onto the layer chosen site. These six samples were wet sieved in mesh sizes 500, 125, and 63 µm. Of all the six samples only one single black grain was larger than 500 µm, it was located at 208-209cm depth in GC-193. The fraction between 500 and 125 µm was primarily examined in microscope to obtain a desired amount of planktonic foraminiferal tests, while the fraction between 125 and 63 µm was in case there wasn't a sufficient number of tests found.

According to *Beta Analytic*™ (2015) 3 to 7 mg of foraminifera carbonate test is needed to produce an accurate carbon date. In the end, it was only the interval 105-106 cm in GC-193 that produced enough material to be dated (23.4mg) (see *Figure 5*), in fact the fraction between 500 and 125 µm was almost entirely made up of *G. Pachyderma* tests. In contrast was no planktonic test found in the interval 208-209 cm in GC-193, not even in the 125-63 µm fraction. The second largest amount of foraminiferal tests was in the interval 148-151 cm in GC-191 weighing in at 0.7 mg, this was the result after the decision was made to collect additional sediment one cm up and below the original interval of 149-150cm. The same expansion of an interval was also attempted with the interval 150-153 cm in GC-193 without

success.

Figure 5. The planktonic foraminiferal tests (125-500μm) used to date the interval depth of 105-106cmbsf in GC-193 as seen through a microscope lens, taken on a cellphone. The legend is calculated from on the diameter the sample slide of 11mm.

23.4 mg sample of planktonic foraminifera tests from 105-106cm interval in GC-193 was shipped to *Beta Analytic*™s laboratory in Miami, FL. USA. At their lab the sample was cleaned by ultrasound in de-ionized water, before being run through an accelerated mass-spectrometer. The result of this was sent in a report as uncorrected and corrected ages.

5 Results

5.1 Core lithostratigraphy

The gravity core located closest to the Aurora vent field is HACON19-GC113 (*Figure 6*), located roughly 100m north of the vents an at a slightly shallower depth of 3892 m compared to the vent field where the blade cores were sampled at 3886 m. Visual description and X-ray imaging was not performed on GC113 because it was part of a preliminary study, but there

are clear downcore changes in color that at some depths match with variations in MS and fractional porosity. The uppermost section of GC-113 is substantially darker than the rest of the core (*Figure 6*). This darker interval coincides to the strongest magnetic signal of over 270, while FP returned anomalously-high values around 1 and was not included in *Figure 6*. Seven more peaks in MS are clearly distinguishable further down at 39 cm, 64 cm, 91 cm, 128 cm, 175 cm, 190 cm and 204 cm bsf, of which the only other interval with values exceeding 150 (MS SI x 10^-5) is between 125 and 132 cm bsf. Slight peaks in FP are also found at the depths 39, 64 and 204 cm.

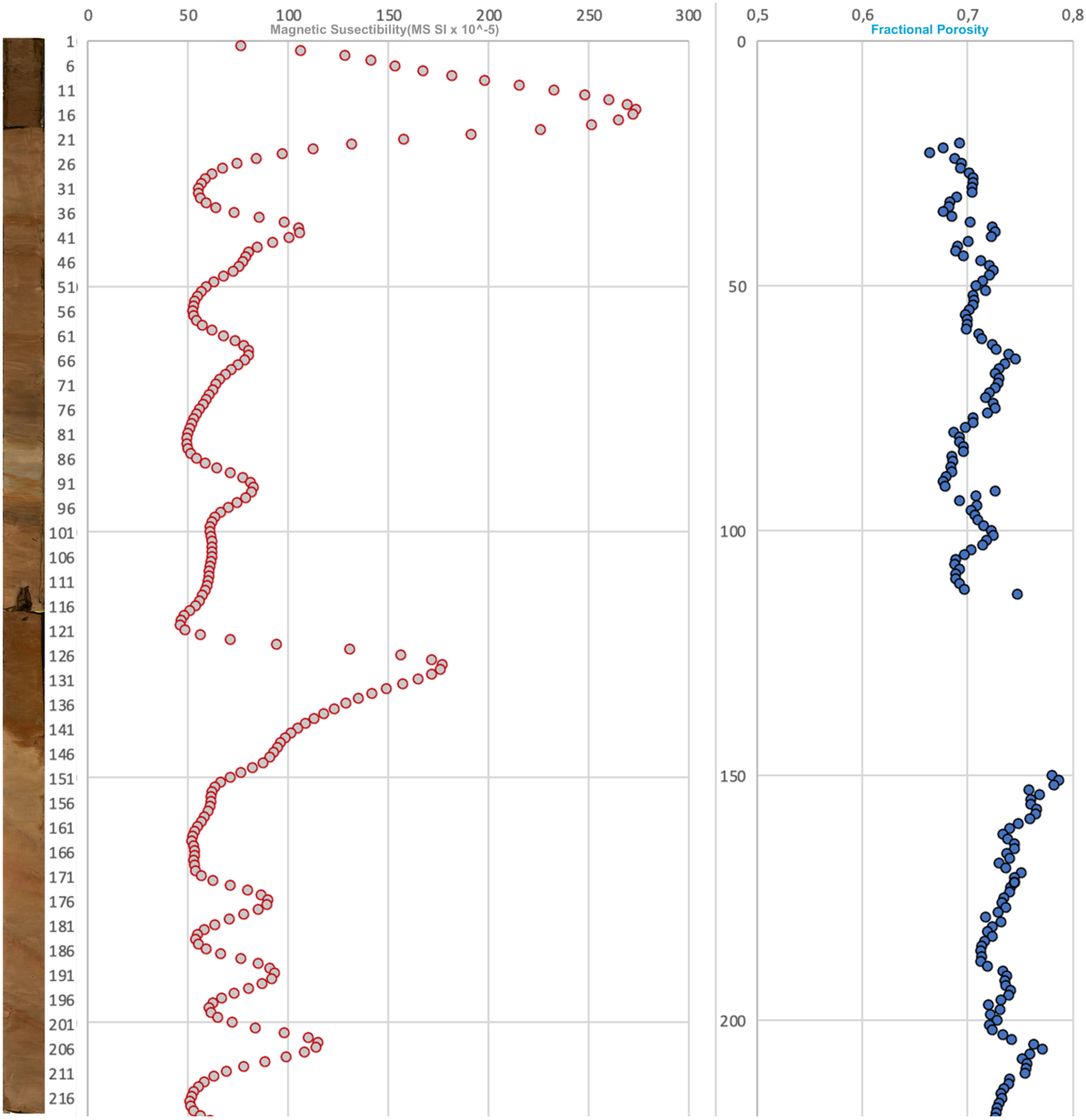

Figure 6. HACON19-32-GC-113, to the left in the figure is the undistorted section images of the core with the seabed surface at the top, side by side the MS and FP measured by MSCL at the same depths.

GC-191 (see *Figure 7*) was sampled 2,4 km north-north-west of the AVF, and is located 63 m deeper, but at the opposite side of the Aurora seamount's summit. No noticeable changes in grain size could be seen in GC-191 during visual inspection. The first core section (0-25 cm) includes two darker layers with the upper located at around 7 cm seeming to dip at a higher angle than the lower one located at 13 cm. All layers in section 2 of GC-191(24-119 cm) are tilted around 15º. In section 3 there is a thin layer at 135 cm with a hue of yellow-red tilted at 7°, other layers deviate less from the plane parallel. The core has the Munsell color 2.5Y5/3 dominating from 25-105 cm, 2.5YR5/2 from 105-165 cm and 2,5Y5/2 from 165 cm to the

core bottom. Depths with a notable correspondence between a visible layer with yellow-red hue and a darker X-ray layer are 61, 68 and 88 cm, these same depths also coincide with peaks in MS above 100 and a relatively stable FP ratio between 0,65 and 0,70.

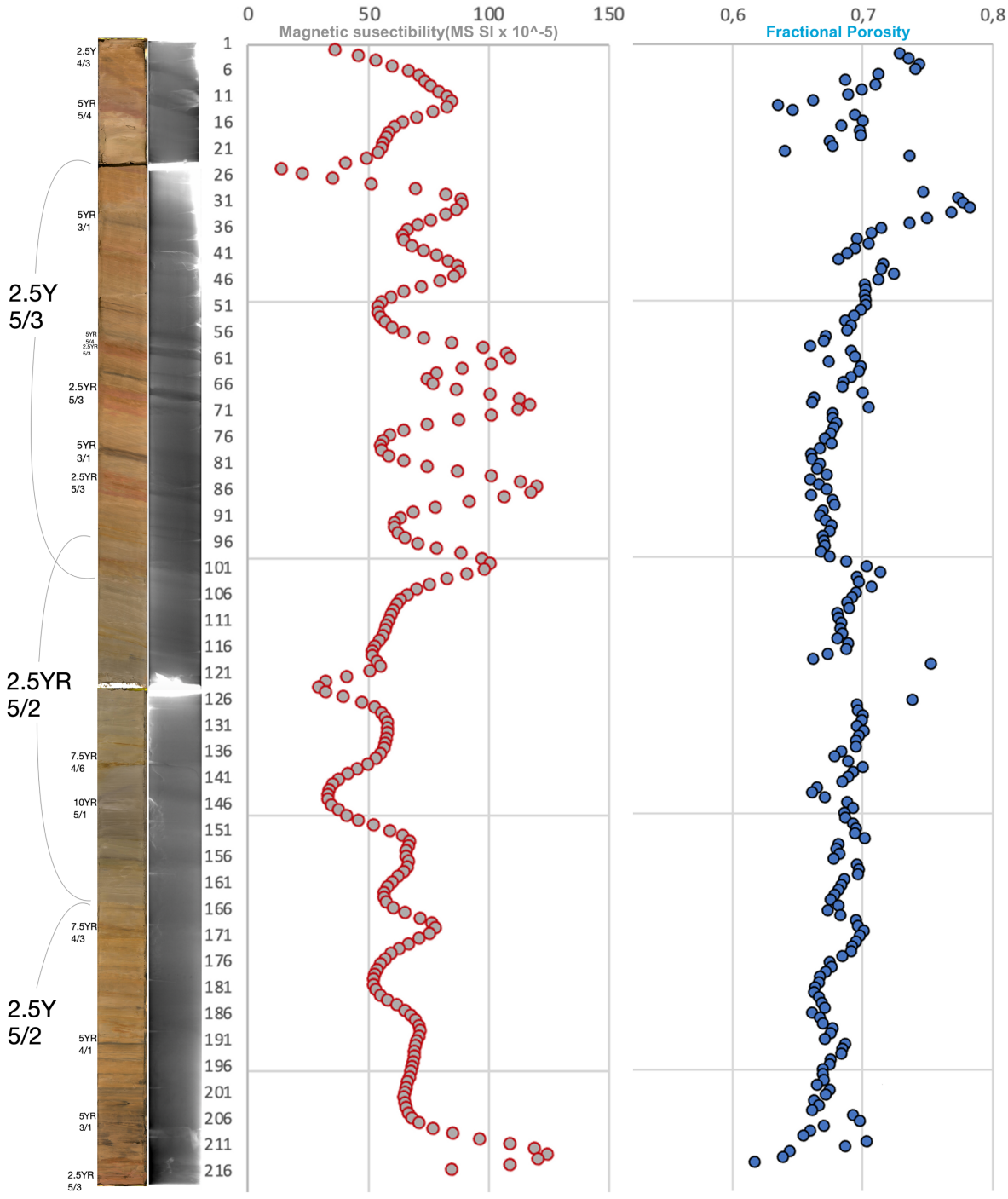

Figure 7. CAGE-KH-HACON21-02-GC-191, to the left in the figure is the undistorted photographic and X-ray images of the core sections with the seabed surface at the top, side by side the MS and FP measured by MSCL at the same depths.

GC-193 (see *Figure 8*) was taken from the southern slope of the Aurora seamount 23 m deeper than, and 400 m south of the AVF. The upper 58 cm of GC-193 has no sedimentary structures could be reliably observed, whilst the grainsize were no bigger than clay or silt, the X-ray of this section seem to support this observation. The entire length of the first section appears as one single MS amplitude with the peak at 29 cm, while FP ratio decreases towards 58 cm. The Munsell color 2.5Y4/4 dominates the upper 82 cm bsf, being replaced by the brighter 2.5Y6/3 for the remaining part. Again, the yellow-red layers match some of the MS peaks at the depths 116, 127, 146, 186 and 205 cm bsf. One dark grey layer (2,5YR3/2) at 139 cm has a particularly low MS and a slight dip in FP. There are fewer layers that are dark, black or gray in GC-193 than in GC-191. Around 86 cm two darker layers appear concorded, immediately below between 92 and 95 cm is a faint truncational surface of red lamina. Comparison between *Figures 7 & 8* suggest that laminations in GC-193 have a higher angle than those described in GC-191, in section 2 of the GC-193 (57-156 cm) reach maximum tilt of 20º below 100 cm, while in section 3 (>156 cm) the recorded tilt angles are largely around 30º.

One successful carbon dating was conducted on GC-193 at the interval 105-105 cm (yellow star in *Figure 8*), this yielded an age of 23850±80 when uncorrected, but when corrected against three marine references (Funder, 1982; Håkansson, 1973; Mangerud, & Gulliksen, 1975) in a calibration curve (Heaton et al., 2020) the one simga age range became 27123 to 27344 cal.yr. BP.

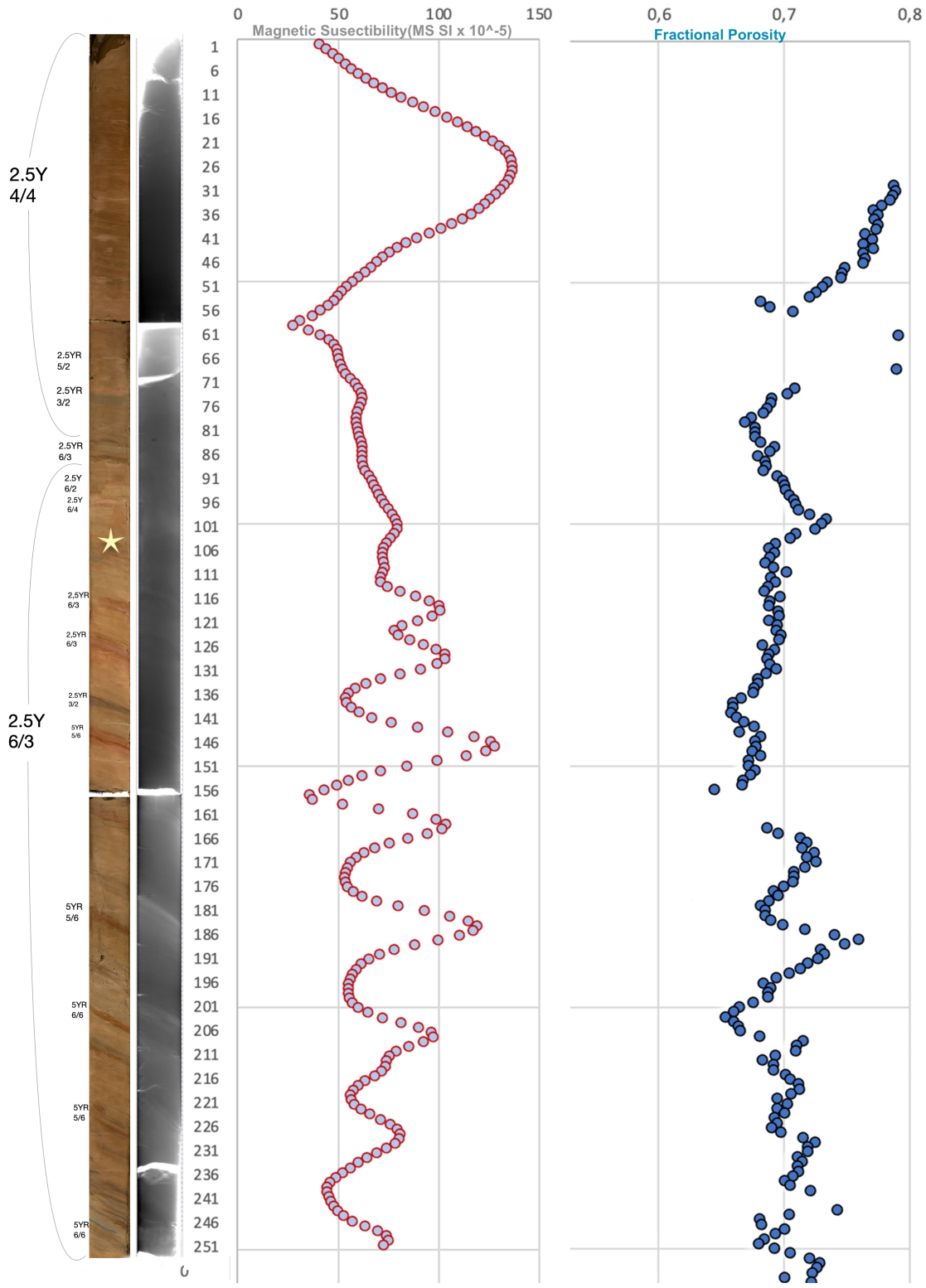

Figure 8 . CAGE-KH-HACON21-02-GC-193, to the left in the figure is the undistorted photographic and X-ray images of the core sections with the seabed surface at the top, side by side the MS and FP measured by MSCL at the same depths. The yellow star from 105-106 cm bsf signifies the one successful carbon dating on the cores.

GC-124 (*Figure 9*) was retrieved from the Lena Trough approximately 40 km west of the main rift. GC-124 was not visually inspected as it was part of a preliminary study with GC-113, but the high-resolution image of the core bear witness of dynamic change to the sedimentary history. At 27, 158, 179-181 cm bsf grains up to the size of sands can be recognized from high-resolution core images. 73 cm bsf contain flame structures of a yellow-red layer beneath against a darker layer above, this can also be observed at 267 cm between a yellow-red and yellow-gray. 222-233 cm and possibly between 290 and 300 cm bsf seem to contain some grains up to the size of very coarse sand, supported be the matrix. Between 340 and 360 cm bsf the yellow-red gradually becomes darker until reaching something akin to 5Y1/2. From the shift at 340 cm down to 400 cm bsf most layers look like clay in the high resolution image. From 400 to 425 cm the sediments appear muddy with weakly toned red-grey color.

Fluctuations, largely between 50 and 150 SI(10^{-5}) MS appear in the upper part of the core, yellow-red layers mostly coincide with the highest peaks and dark to light yellowish layers with bottoms. The dark interval between 350 to 400 cm bsf contain particularly low MS values of around 30-40, and lower porosity compared to the overlying units. A correspondence between higher MS and a lower FP is identified at the depths 15, 33, 49, 85, 176, 221, 236 and 258 cm bsf, with the inverse relationship of low MS and high FP at the depths 26, 55, 95, 151, 204, 228 and 280.

The gravity cores in *Figure 10* were not split open, therefore only MS and FP will be presented. GC-107, GC-110 and GC-115 have a strong positive, long wavelength MS between 3 to 54 cm bsf, 42 to 75 cm bsf, and 44 to 75 cm bsf respectively, of which GC-110 and GC-115 have strong negative MS values between the seabed and the aforementioned. Except for some noise the cores with the clearest trend of gradually smaller FP with depth are GC-110, GC-116 and GC-122. The exceptionally strong MS peaks seem to generally correlate with lower FP ratios across all cores in *Figure 10*.

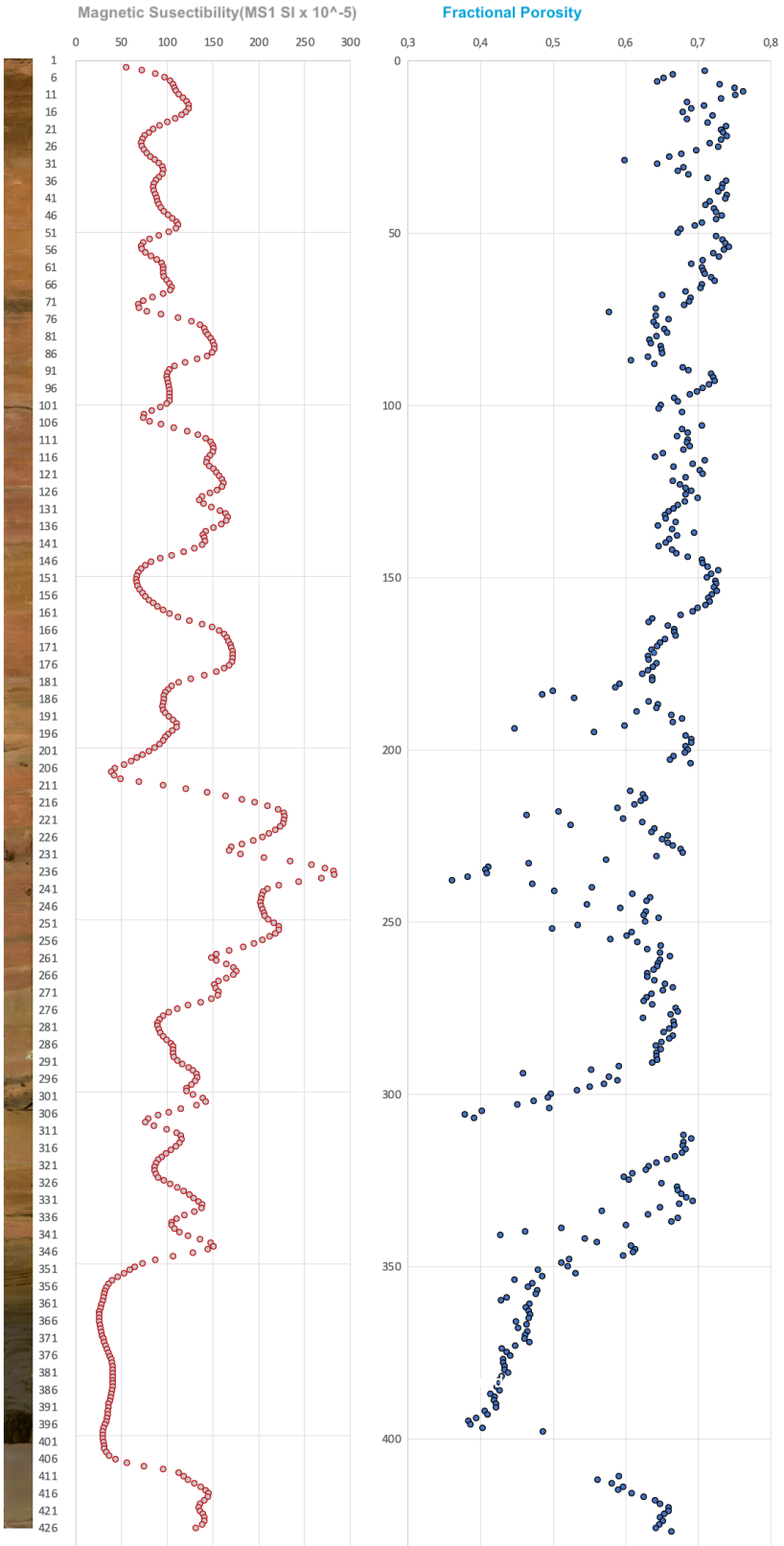

Figure 9. HACON19-GC124, to the left in the figure is the undistorted section images of the core with the seabed surface at the top, side by side the MS and FP measured by MSCL at the same depths.

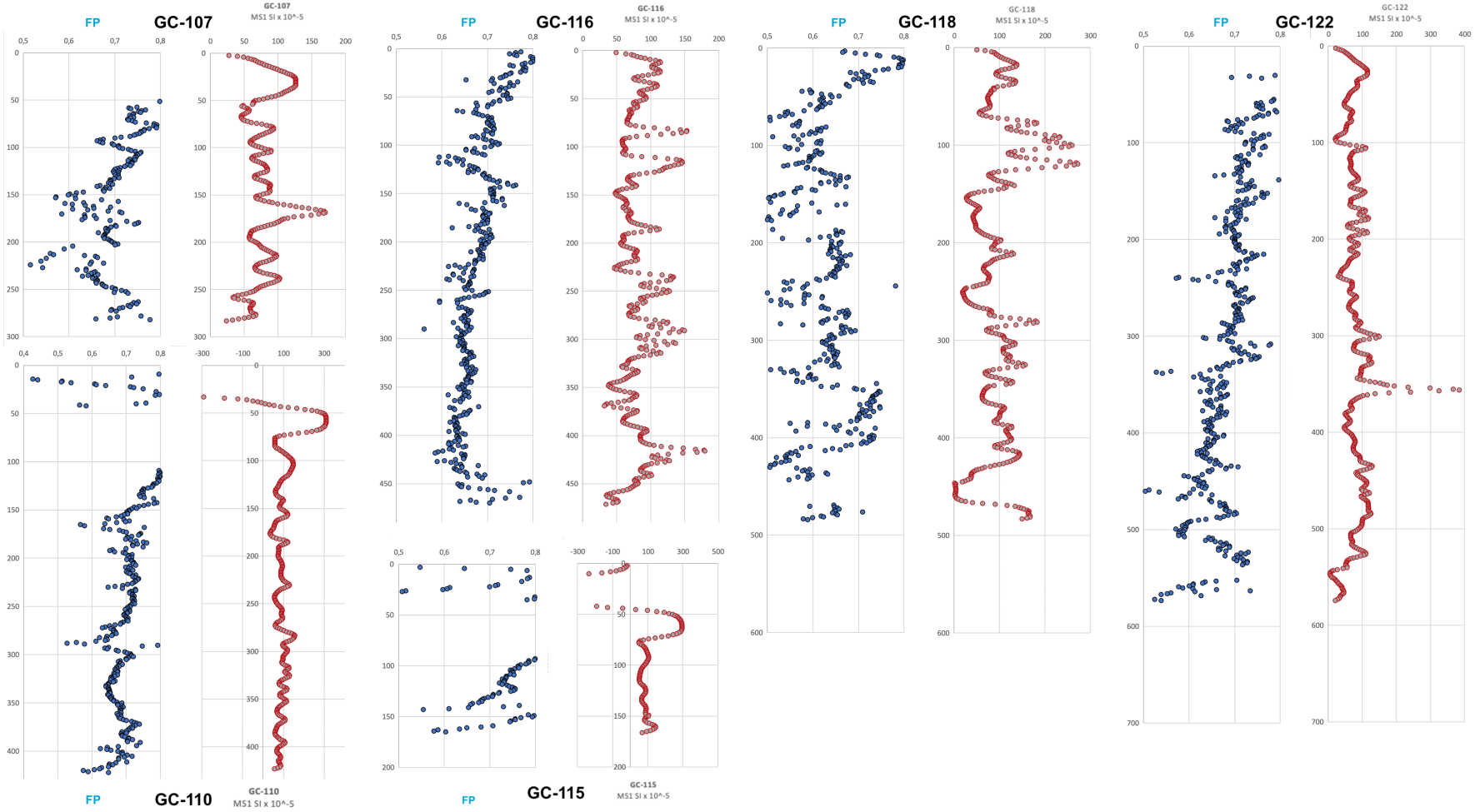

Figure 10. HACON19 gravity cores MS(red) and FP(blue) as measured by MSCL at the same depths.

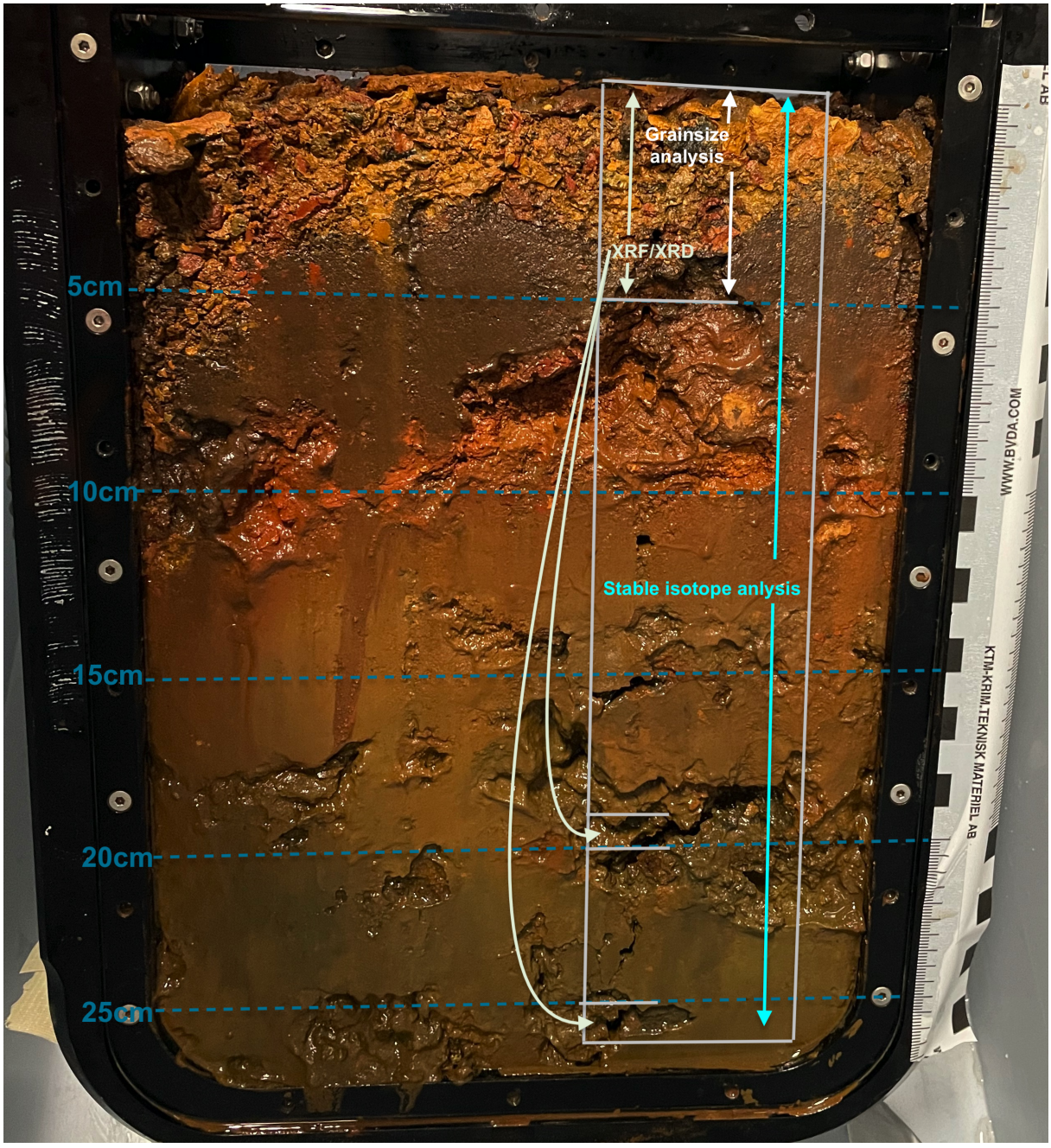

Figure 11. Picture of HACON21-BlaC01 before sampling. The cyan arrows highlights the extent of depth of samples collected for stable isotope analysis (Figure 15). The upper 5 cm were also analyzed the distribution of grainsizes (Figure 13). The upper 5 cm as well as the intervals 19-20 cm and 25-26 cm highligth the depths geochemically analysed (see Table 3 & 4). The left part of the core not highlighed were samples allocated for other research (Bunz & Ramirez-Llodra, 2021). Edited from photograph taken by Sofia Ramalho.

Figure 11 suggests the upper 3.5 cm of BlaC01 contain less matrix between the debris and clasts, with the pore space gradually becoming filled with smaller particles. Several of the rock samples of chimney debris collected during HACON21 were so brittle that they that they

quickly broke into smaller pieces (Bunz & Ramirez-Llodra, 2021), therefore it is hard to determine if a piece is truly in the size range of pebble or just smaller pieces that are loosely attached. The upper 5 cm appear to fall within the hue of 7,5YR of the Munsell color wheel, while the 6 to 13 cm have a redder hue of 2,5YR, around 25 cm the matrix color becomes more neutral, but retaining some yellow-red hue.

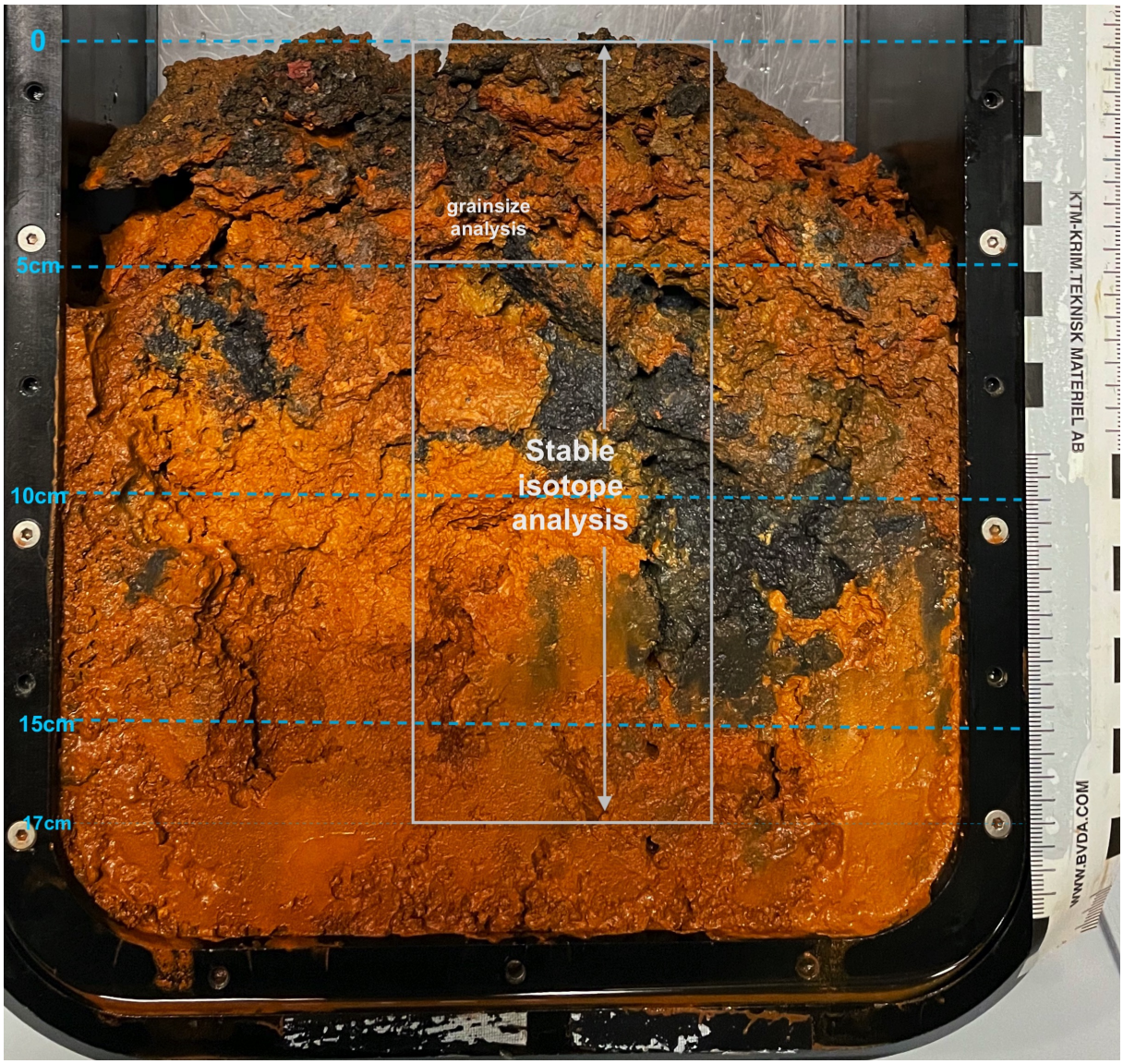

Figure 11. Picture of HACON21-BlaC03 before sampling. The grey rectangle outline highlights the depth range of samples collected for stable isotope analysis (Figure 15). The upper 5 cm were also analyzed the distribution of grainsizes (Figure 13). Edited from photograph taken by Sofia Ramalho.

When observing the size of fragments in BlaC03, one can be tempted to describe the largest grainsizes as cobble (>64 mm), but it is uncertain if these would remain as one clast if mobilized. The oxidized surfaces in the blade core are yellow-red varying in hue from 2,5YR to 5YR. The dark surfaces are likely sulfide minerals exposed as a result of the sampling

process and affirming how brittle these clasts are. Clast at the seabed (upper 3 to 4 cm) also have surfaces exposed due to the sampling but appear browner.

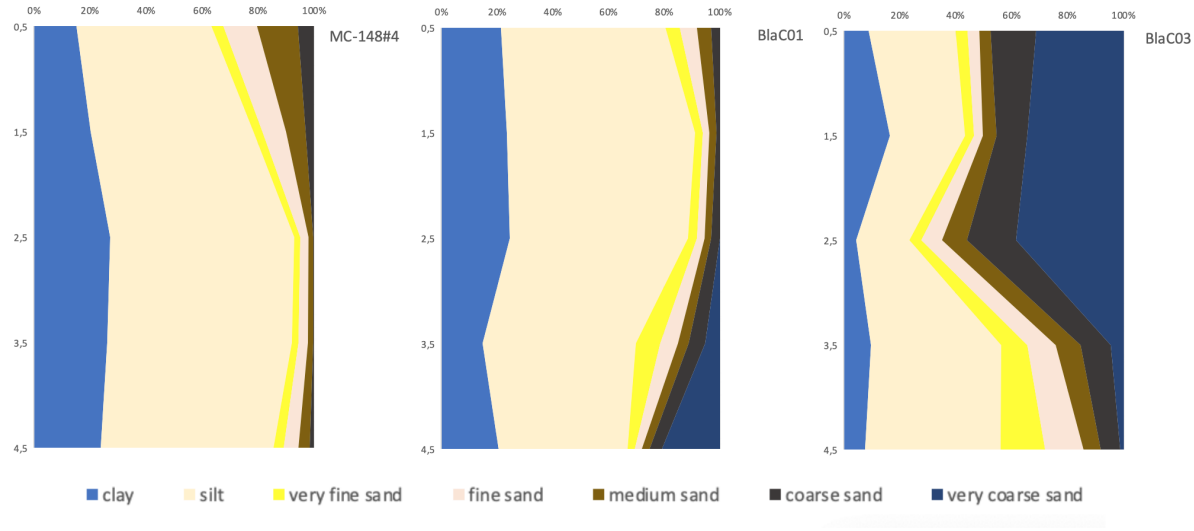

Figure 12. The grainsize distribution the one-cm intervals in the five upper cm of the multicore MC-148#4 from the reference site as well as the blade cores BlaC01 and BlaC03 from the active vents. The grainsizes are divided into the categories less than 2 μm(clay), 2-63 μm(silt), 63-125 μm(very fine sand), 125-250 μm(fine sand), 250-500 μm(medium sand), 500-1000 μm(coarse sand) and 1000-2000 μm(very coarse sand).

The reference MC-148#4 (see *Figure 12*) is dominated by clay and silt, making up to 93 % of the sediment in the uppermost 5 cm. Only 0.16 % very coarse sand was detected in the interval 4 to 5 cm, and coarse sand typically a few percent, except for at the surface where it was nearly 6 %. Overall, there was slightly less very fine sand compared to fine and medium sand sizes in MC-148#4.

BlaC01 shows some similarities in grainsize with the reference site in the upper 3 cm, but with very coarse sand increasing from 3 to 5 cm bsf, from 0 to 21 %, and very coarse sand being as high as 6 % in 3-4 cm.

The largest grain size fraction in BlaC03 is very coarse sand from 0 – 3 cm, making up 34 to 38 %, and is replaced by silt as the dominating fraction from 3 to 5 cm. The fractions of fine, medium, and coarse sand are notably higher, with averages of 7.7, 6.5 and 12.5 % from 0 to 5 cm in BlaC03.

5.2 Core geochemistry and mineralogy

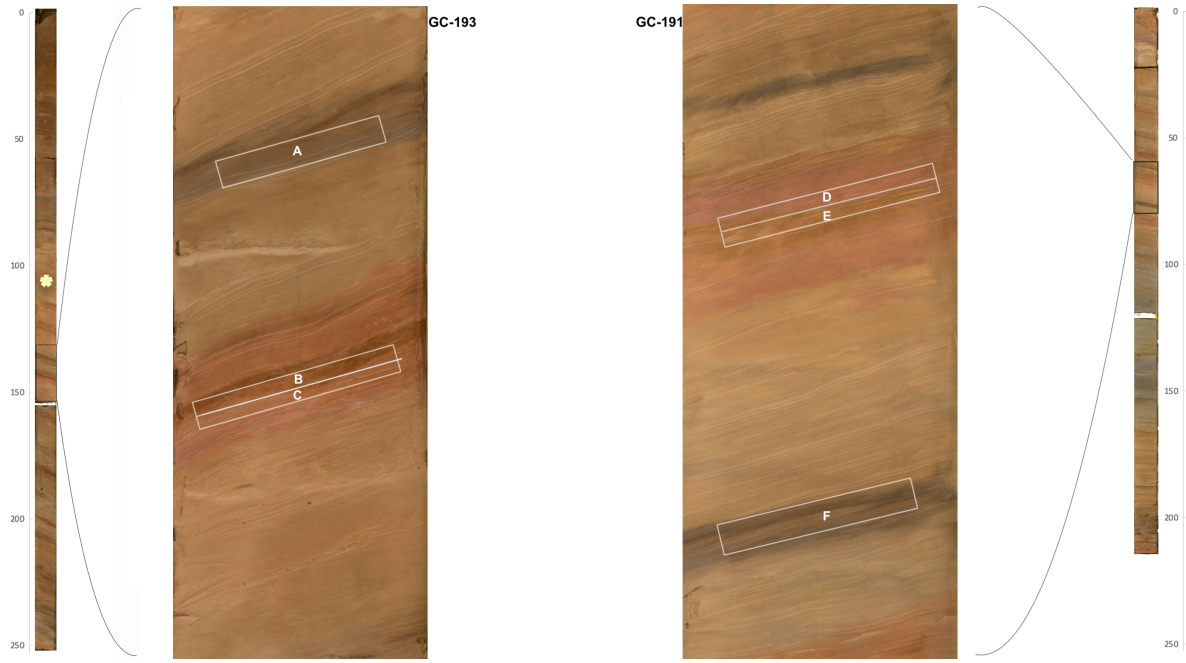

Figure 12. Sites chosen for major and trace element analysis from cores HACON21-GC-193 (left) at the depth intervals 131-132cm (A), 139.5-140.0cm (B) and 140.0-140.5cm (C), and HACON21-GC-191 (right) at 67.0-67.5cm (D), 67.5-68.0cm (E) and 78-79cm (F). Yellow star is site of the carbonating.

The gravity cores display a vibrant collection of Munsell colors, the hue of the color may change slightly from one lamina to the next while remaining in the same tone and saturation. Information about the geochemical composition of distinctly different beddings, may allow us to separate lithological units and establish a temporal order of the environmental changes and hydrothermal activity. The composition of the sediment will help us identify plume deposits along the cores. Therefore, we selected intervals to be sampled for their precise chemical and mineralogical composition, *Figure 12* highlights these intervals with XRF(chemical) and XRD(mineralogical) results listed in the tables below.

5.2.1 XRF

Table 1. Major elements detected by XRF in samples from the gravity cores as pointed in Figure 10. Loss on Ignition (LOI) of volatiles at a temperature of 1050°C is also given as a percentage of original sample mass.

	LOI 1050*	SiO2	TiO2	Al2O3	Fe2O3	MnO	MgO	CaO	Na2O	K2O	P2O5
	%	%	%	%	%	%	%	%	%	%	%
A	8,77	53,42	0,87	17,18	6,87	0,36	3,25	2,19	2,28	3,66	0,22
B	10,25	53,58	0,66	13,37	7,03	0,18	4,42	4,42	1,79	3,53	0,22
C	10,58	52,20	0,66	14,60	8,37	0,19	4,31	4,36	1,91	3,51	0,27
D	10,43	51,32	0,73	15,42	7,60	0,44	3,91	3,96	2,08	3,58	0,23
E	10,72	52,17	0,67	13,24	6,05	0,38	4,28	5,54	1,65	3,43	0,18
F	8,45	54,98	0,86	16,85	6,58	0,83	3,26	1,92	2,16	3,67	0,22

Si, Ti, and Fe have small variations across the samples, with dark grey having slightly more of Si and Ti. The reddish samples (B, C, D & E of *Figure* 12) appear to contain less Al than the dark-grey layer A and F layers. Layer F has the highest Mn content of any at 0,83 %, with all samples from GC-191 being higher than those of GC-193. Ca is 2-3 times higher in B, C, D and E, than A and F, with values up to 5,54 %. B and E have with a small margin the highest concentrations of Mg, and slightly less Na with a maximum difference of only 0.63%. The dark grey samples A and F have around 2 % less weight that were LOI than the reddish samples.

Table 2. Minor elements detected by XRF in samples from the gravity cores as pointed in Figure 10

	Ba	Co	Cr	Cu	Ni	Sr	Zn	Zr
	µg/g	µg/g	µg/g	µg/g	µg/g	µg/g	µg/g	µg/g
A	419	< 50	< 50	< 100	< 50	170	< 100	188
B	365	< 50	179	< 100	55	122	< 100	144
C	317	< 50	301	< 100	90	126	< 100	149
D	443	< 50	< 50	< 100	74	135	< 100	180
E	386	< 50	< 50	< 100	< 50	112	< 100	191
F	445	51	120	< 100	< 50	159	< 100	159

A, D and F have Ba values exceeding 400 µg/g, while sample C is nearly 300 µg/g. F has the only accurate reading of Co at 51 µg/g. C has a relatively higher measurement of Cr at 301 µg/g, with all other samples other than B having less than half. C also contain significantly more Ni, followed by D and B. However, A and F have slightly higher concentration of Sr. The dark layer of GC-193 have a higher concentration of Zr than the red brown, but the opposite is observed in GC-191.

Table 3. Major elements detected in the upper 5 cm as well as 19-20 and 25-26 cm depth of BlaC01.

	LOI 1050°C	Cl	S	Fe2O3	Fe	Cu	CaO	Al2O3	SiO2	MgO	K2O	MnO	TiO2	Na2O	P2O5	Ba
BlaC01 (cm)	%	%	%	%	%	%	%	%	%	%	%	%	%	%	%	%
0,5	16,5097	2,73	2,93	56,05	39,18	7,67	0,91	1,73	8,19	2,03	0,45	0,35	0,10	3,41	0,78	< 0,05
1,5	22,0207	3,56	1,85	43,38	30,32	11,84	0,77	2,22	10,68	2,98	0,41	0,92	0,12	3,50	0,68	< 0,05
2,5	23,5295	3,18	1,43	46,93	32,80	10,10	0,81	2,47	10,88	1,72	0,41	0,39	0,14	3,30	0,67	< 0,05
3,5	22,7315	2,9	0,89	51,07	35,70	5,55	0,71	3,09	12,56	1,52	0,41	0,17	0,16	3,06	0,59	< 0,05
4,5	20,1673	2,96	0,93	53,50	37,40	7,25	0,66	2,50	11,14	1,77	0,32	0,27	0,13	2,77	0,55	< 0,05
	LOI 1050°C		S		Fe2O3	Cu	CaO	Al2O3	SiO2	MgO	K2O	MnO	TiO2	Na2O	P2O5	Ba
	%				%	%	%	%	%	%	%	%	%	%	%	%
19,5	15,9814		2,1		53,79	3,72	0,38	2,74	13,96	3,27	0,62	< 0,05	0,15	3,06	1,01	0,01
25,5	14,6156		18,2		64,83	9,75	0,12	0,72	4,53	1,35	0,19	< 0,05	< 0,05	1,42	0,47	< 0,01

In BlaC01 (*Table 3*) sulfur was detected with a slight increase in concentration towards the surface (0,5 cm) but is less than six times the concentration of sulfur at 25-26 cm. Cu varied with nearly half from 2,5 to 3,5 cm, roughly between 6 % and 12 %, but lowest concentration of less than 4 % was at 19,5 cm. Al and Si were quite low, with concentrations no higher than 3,1 and 12,6 % respectively. An element that appears to display a gradient is phosphor, that decreased from 0,78 to 0,55 % from 0 to 5 cm depth, but the highest concentration of 1 % was located in 19-20 cm bsf. The concentrations of Si, Ti, Mn, Ca, K, and P are the lowest at

25-26 cm depth among all samples from BlaC01, with the same interval having the highest concentrations of Co, Zn as seen *Table 4*.

Table 4. Minor elements detected in the upper 5 cm cm as well as 19-20 and 25-26 cm depth of BlaC01.

	Zn	Co	Cr	Sr	V	Zr
BlaC01 (cm)	µg/g	µg/g	µg/g	µg/g	µg/g	µg/g
0,5	405	980	< 50	< 100	205	< 10
1,5	292	1824	< 50	< 100	182	14
2,5	314	735	< 50	< 100	201	17
3,5	348	322	< 50	< 100	168	20
4,5	255	503	< 50	< 100	156	13

	Zn	Co	Cr	Sr		Zr	Ni	Pb
	µg/g	µg/g	µg/g	µg/g		µg/g	µg/g	µg/g
19,5	892	106	< 50	< 100		< 50	36	254
25,5	2645	942	< 50	< 100		< 50	36	85

Vanadium and zink have the highest concentrations in the surface sediment(0-1 cm), and cobalt the highest between 1 and 2 cm, other elements appear either with random or qualitative values in *Table 4*.

The only quantitative measurement of lead(Pb) in this thesis and only measurement of nickel(Ni) in the blade and multi cores were done at 19-20 and 25-26 cm depth in BlaC01, Pb varies 3-fold, while Ni shows no variation.

Table 5. Major elements detected in the upper 5 cm of BlaC03. n.m.=not measured

	LOI %	Cl	S	Fe2O3	Fe	Cu	CaO	Al2O3	SiO2	MgO	K2O	MnO	TiO2	Na2O	P2O5	Ba
BlaC03	1050°C	%	%	%	%	%	%	%	%	%	%	%	%	%	%	%
0,5	16,2687	1,38	1,59	65,64	45,88	2,50	0,55	0,68	8,32	2,75	0,19	< 0,05	0,04	1,63	0,63	< 0,05
1,5	16,1662	1,54	0,74	68,35	47,78	1,23	0,35	0,66	7,51	2,67	0,14	< 0,05	0,04	1,73	0,76	< 0,05
2,5	12,7071	1,47	3,53	53,60	37,47	7,83	0,32	0,93	12,13	6,05	0,23	< 0,05	0,05	1,85	0,69	< 0,05
3,5	n.m.	1,39	16,17	53,23	37,21	20,24	0,20	0,84	6,70	3,01	0,22	< 0,05	n.m.	n.m.	n.m.	< 0,05
4,5	n.m.	0,44	33,04	55,94	39,1	27,18	0,06	0,03	0,89	0,50	0,05	< 0,05	n.m.	n.m.	n.m.	< 0,05

In *Table 5* of BlaC03, S increases from 0,74 to 33,04 % between 1 and 5 cm, being barely higher in the surface interval 0-1 cm, with something similar being observed for Cu being as low as 1,23 % and as high as 27,18 % from 1 to 5 cm depth. Fe in BlaC03 is consistently slightly higher than in BlaC01(*Table 3*), with absolutely highest concentration between 0 and 2 cm. Ca and Al is lower than 1 %. Si is also beneath 1% in 4-5 cm, but reaches 12% in 2-3 cm. In BlaC03(*Table 5*), K, Na and Ti are in concentrations half of that in BlaC01(*Table 3*), while Mg is slightly higher in BlaC03.

Table 6. Minor elements detected in the upper 5 cm of BlaC03. n.m.=not measured

	Zn	Co	Cr	Sr	V	Zr
BlaC03	µg/g	µg/g	µg/g	µg/g	µg/g	µg/g
0,5	3700	557	< 50	< 100	141	< 10
1,5	4800	521	< 50	< 100	86	< 10
2,5	3200	979	< 50	< 100	72	< 10
3,5	< 500	3349	n.m.	n.m.	n.m.	n.m.
4,5	< 500	7115	n.m.	n.m.	n.m.	n.m.

Zn is around one order of magnitude higher in the samples from BlaC03(*Table 6*) than in the upper 5 cm of BlaC01(*Table 4*). BlaC03 also have the highest concentration of Co of 7115 µg/g from 4-5 cm but has consistently less V and Zr than BlaC01.

Table 7. Major elements detected in the upper 5 cm of MUC-148.

	LOI %	Cl	S	Fe2O3	Fe	Cu	CaO	Al2O3	SiO2	MgO	K2O	MnO	TiO2	Na2O	P2O5	Ba
MC-148	1050°C	%	%	%	%	%	%	%	%	%	%	%	%	%	%	%
0,5	16,9597	2,14	0,48	6,97	4,87	< 0,1	6,97	12,92	44,16	3,45	2,16	0,27	0,69	3,62	0,25	< 0,05
1,5	15,9467	2,1	0,43	7,00	4,89	< 0,1	7,00	13,42	45,28	3,59	2,34	0,27	0,70	3,28	0,24	< 0,05
2,5	14,7089	1,66	0,40	6,83	4,77	< 0,1	6,62	13,35	46,79	3,71	2,63	0,24	0,70	3,01	0,22	< 0,05
3,5	13,947	1,35	0,37	6,66	4,66	< 0,1	6,44	13,27	47,61	3,71	2,68	0,23	0,72	2,81	0,21	< 0,05
4,5	14,8658	1,48	0,41	7,16	5,00	< 0,1	7,33	13,61	46,07	3,24	2,56	0,31	0,73	3,11	0,25	< 0,05

In the upper 5 cm of MUC-148(*Table 7*), S is around 0,4 %, Fe and Ca are around 7 %, Al around 13 %, Si 44-48 %, Mg around 3,5 %, K around 2,5%, Mn and P are around ¼ %, and Ti around 0,7 %. Na concentrations are similar to those in BlaC01. While Cu is practically absent in comparison.

Table 8. Minor elements detected in the upper 5 cm of MUC-148.

	Zn	Co	Cr	Sr	V	Zr
MC-148	µg/g	µg/g	µg/g	µg/g	µg/g	µg/g
0,5	39	< 50	82	304	197	164
1,5	46	< 50	87	291	190	180
2,5	50	< 50	84	254	180	183
3,5	51	< 50	80	247	167	192
4,5	49	< 50	78	354	207	157

Zn concentrations in MUC-148(*Table 8*), is one order of magnitude lower than BlaC01 and two orders of magnitude less than in BlaC03. Co is comparatively lower in MUC-148, whilst Cr, Sr, and Zr are in higher concentrations in MUC-148 compared to the blade cores, and V is nearly the same as in BlaC01.

5.2.2 XRD

Table 9. Minerals from the upper 5 cm of as well as 19-20 and 25-26 cm depth of BlaC01 (see Figure 11).

	Depth	Plagioclases (%)	K-Feldspath (%)	Quartz (%)	Argiles / micas (%)	Goethite (%)	Talc (%)	Amphibole (%)	Halite (%)	Calcite (%)	Dolomite (%)	Chalcopyrite (%)	Atacamite (%)	Isocubanite (%)	Botallackite (%)
		Ca(Na)Al 2Si2O 8	KAlSi3O8	SiO2		Fe(III)OOH	Mg3Si4O10 (OH)2	RSi4O11	NaCl	CaCO3	CaMa(CO3)2	CuFeS2	Cu2Cl(OH)3	CuFe2S3	Cu2(OH)3Cl
BlaC0 1	0.5	2	/	4	48	31	/	/	6	/	/	4	2	/	3
	1.5	8	/	5	34	27	/	/	8	/	/	1	11	/	7
	2.5	<1	/	5	47	22	/	/	8	/	/	1	11	/	7
	3.5	<1	/	8	42	40	/	/	6	/	/	<1	2	/	2
	4.5	<1	/	5	40	37	/	/	7	/	/	<1	7	/	4

	Plagioclases (%)	K-Feldspath (%)	Quartz (%)	Argiles / micas (%)	Goethite (%)	Hematite (%)	Lepidocrocite (%)	Talc (%)	Halite (%)	Calcite (%)	Pyrite (%)	Pyrrhotite (%)	Chalcopyrite (%)
						Fe2O3	FeOOH				FeS		
19,5	<1	<1	6	<1	78	1	3	5	7	<1	<1	<1	1
25,5	<1	<1	2	<1	67	<1	2	<1	4	<1	<1	2	23

Excluding sea salt, the mineralogy of the upper 5 cm of BlaC01(*Table 11*) is dominated in the following order argiles/micas, goethite, atacamite, quartz, botallackite, plagioclases and chalcopyrite. While deeper down in the same blade core(*Table 12*) in the samples G(19-20 cm) and H(25-26 cm) Argiles/micas are almost absent, while iron oxide-hydroxides, mainly goethite dominated roughly between 70 to 80 % of the mineralogy, followed by pyrites, quartz, talc, and hematite.

Table 10. Minerals from the upper 5 cm of BlaC03.

	Depth	Plagioclases (%)	K-Feldspath (%)	Quartz (%)	Argiles / micas (%)	Goethite (%)	Talc (%)	Amphibole (%)	Halite (%)	Calcite (%)	Dolomite (%)	Atacamite (%)	Chalcopyrite (%)	Isocubanite (%)	Botallackite (%)
		Ca(Na)Al 2Si2O 8	KAlSi3O8	SiO2		Fe(III)OOH	Mg3Si4O10(OH)2	RSi4O11	NaCl	CaCO3	CaMa(CO3)2	CuFeS2	Cu2Cl(OH)3	CuFe2S3	Cu2(OH)3Cl
BlaC03	0.5	/	/	1	23	64	5	/	1	/	/	4	2	<1	/
	1.5	/	/	1	<1	93	4	/	2	/	/	<1	<1	<1	/
	2.5	/	/	2	<1	89	5	/	4	/	/	<1	1	<1	/
	3.5	/	/	2	15	38	20	/	4	/	/	2	17	1	/
	4.5	/	/	<1	<1	7	3	/	3	/	/	<1	83	4	/

The occurrence of goethite is around 90 % between 1-3 cm in BlaC03(*Table 10*) but is replaced as the dominant mineral in 4-5 cm by chalcopyrite at 83 %. Argiles/micas, talc and atacamite are highly variable in concentration, while quartz only reaches a couple of percent.

Table 11. Minerals from the upper 5 cm of MC-148.

	Depth	Plagioclases (%)	K-Feldspath (%)	Quartz (%)	Argiles / micas (%)	Goethite (%)	Talc (%)	Amphibole (%)	Halite (%)	Calcite (%)	Dolomite (%)	Atacamite (%)	Chalcopyrite (%)	Isocubanite (%)	Botallackite (%)
		Ca(Na)Al 2Si2O 8	KAlSi3O8	SiO2		Fe(III)OOH	Mg3Si4O10(OH)2	RSi4O11	NaCl	CaCO3	CaMa(CO3)2	CuFeS2	Cu2Cl(OH)3	CuFe2S3	Cu2(OH)3Cl
MC-148	0.5	13	5	17	42	/	/	3	5	10	5	/	/	/	/
	1.5	15	6	18	41	/	/	3	4	9	5	/	/	/	/
	2.5	11	6	21	42	/	/	3	4	8	5	/	/	/	/
	3.5	12	6	20	42	/	/	3	3	8	5	/	/	/	/
	4.5	14	6	18	42	/	/	3	4	10	4	/	/	/	/

In MUC-148(*Table 11*) the dominant mineral species are in decreasing order, clay species, quartz, feldspars, carbonates, and amphibole, when sea salt is excluded.

MUC-148 have comparatively less variation across its upper 5 cm than the blade cores, with is dominant mineral species being practically absent from the vent field.

5.2.3 Stable Isotope Analysis

BlaC01 (*Figure 13*) have Total Organic Carbon (TOC) percentage of weight (wt%) varying from 3,53 to 0,07 %. δ13C(‰,VPDB) increases from just under -31 in the surface to -24,56 ‰ in 24-25 cm bsf in BlaC01.

The TOC of BlaC03 peaks at 2,5 cm depth and reaches its smallest measured value at 6,5 cm of 1,52 and 0,17 wt% respectively. δ13C(‰,VPDB) is around -30 from 0 to 9 cm depth, and increases to nearly -20 at 10-11 cm, varying slightly between -20 and -25 down the rest of BlaC03.

MUC-148 has the smallest variation in TOC, between 0,82 and 1,47 wt% see *Figure 13*. δ13C(‰,VPDB) is relatively constant compared to the blade cores, with an average of -23,86.

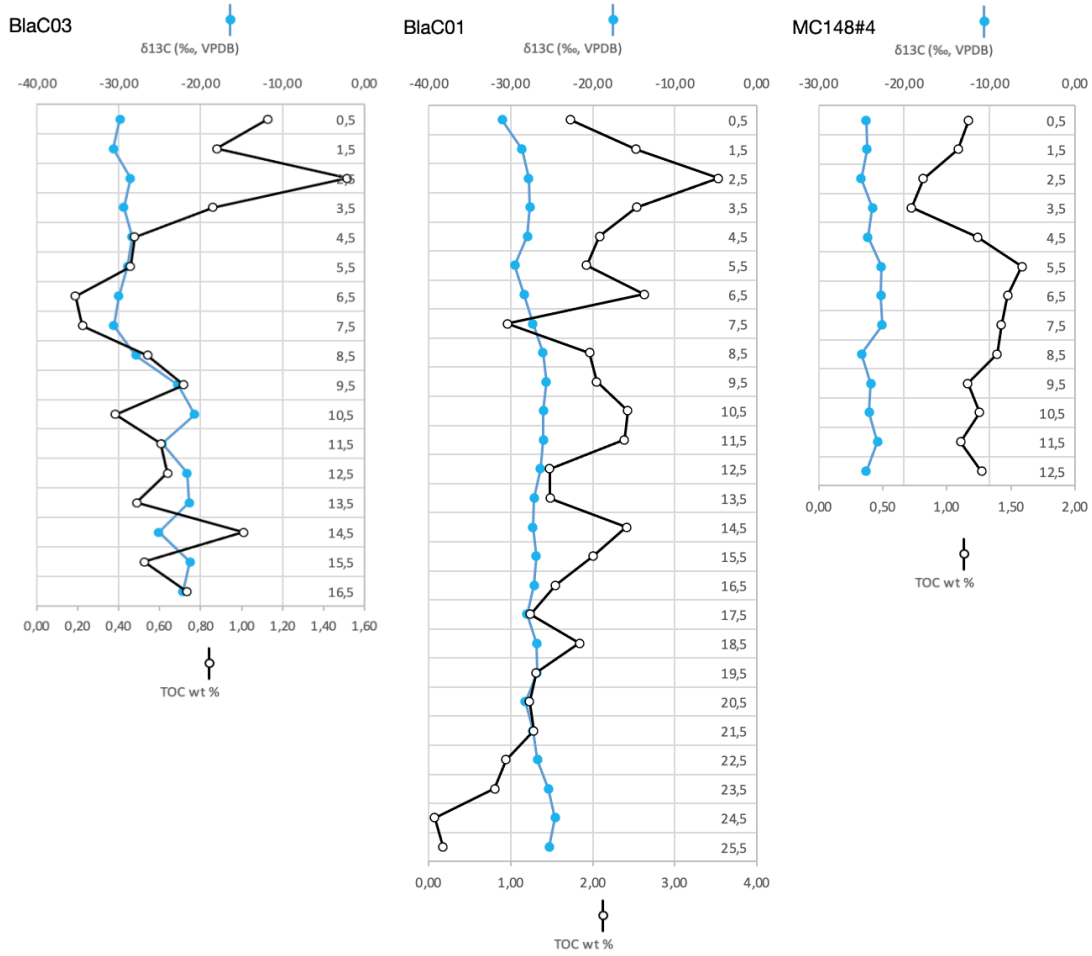

Figure 13. Distribution of the percent of TOC and the permille deviation of ^{13}C content compared to the Vienna Peedee Belemnite isotope reference in sediment samples from every 1cm intervals from seabed surface down to the depth of 17cm, 26cm and 13cm in BlaC03, BlaC01 and MC148#4 respectively.

BlaC01(*Figure 14*) have intervals with the highest Total Organic Nitrogen (TON) percentage than any of the cores being as high as 0,403 % and 0,395 % from 1-3 cm bsf, then varying around 0,2 to 0,3 % from 3 to 17 cm bsf, when it gradually decreases to a minimum of 0,01% at 24-25 cm. The graph of δ15N(‰, N_2air) appear to have a trend increasing values downcore from 2,80 to 5,82 ‰ at 0-1 and 24-25 cm (Sample H in *Table 5, 6 &12*).
BlaC03 also have indications of a trend of decreasing TON concentrations with depth with the highest values at 0,5 and 2,5 cm bsf and the lowest at 15,5 cm, from 0,19 to 0,02‰. In BlaC03 the lowest and highest δ15N(‰, N_2air) are all between 6 and 9 cm bsf going from 1,38 up to 5,03 and down to 1,34 ‰. In the upper 3 cm of BlaC03 δ15N(‰, N_2air) is above 4, whilst beneath 9 cm bsf it is less than 2 ‰.
In MUC-148 TON is in concentrations is lower than BlaC01 and higher than BlaC03 at the same depth intervals, from 0,10 to 0,16 between 3,5 and 5,5 cm bsf. δ15N(‰, N_2air) is slightly higher than BlaC01 and particularly higher than BlaC03 and varies only with 1 ‰, going from 5,42 to 6,43, between 3,5 and 7,5 cm bsf respectively.

The organic C/N (atomic) ratio in BlaC01 varies between 4,79 and 9,60 between 7 and 9 cm depth, all other intervals in the blade core are within this range. BlaC03 have the largest variation in C/N ratio between 4,31 and 23,66, with the upper 9 cm showing similar trends to that of BlaC01. Lastly MC-148 of the reference site display the least variation in C/N ratio, being between 6,01 and 6,99.

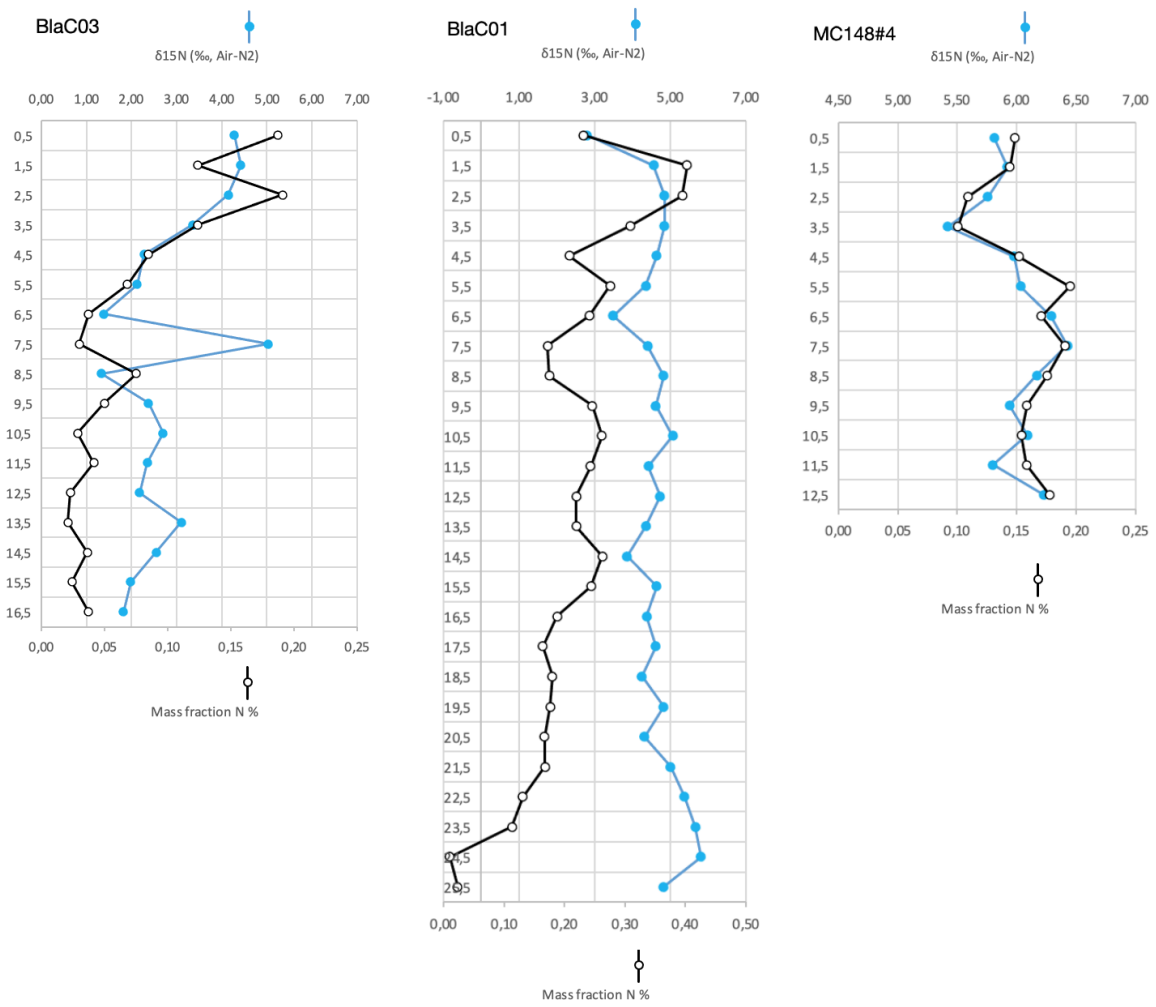

Figure 14. Distribution of the percent of TON and the permille deviation of ^{15}N content compared to atmospheric N_2 as an isotope reference in sediment samples from every 1cm intervals from seabed surface down to the depth of 17cm, 26cm and 13cm in BlaC03, BlaC01 and MC148#4 respectively.

5.3 Pore fluid geochemistry

The headspace extracted displays relatively small concentrations of methane at the various depths of different types of cores at distal and proximal positions relative to the AVF. 25 cm depth in GC-191 and 150 cm depth in GC-193 (see *Table 12*) even have concentrations in headspace gas below that of the modern atmospheric methane concentration of 1,9 ppm (NOAA, 2023).

Table 12. The Concentrations of methane detected in the headspace gas from BlaC01 in the vent field and the gravity cores in proximity to the AVF.

Core, Depth	Parts per million (ppm)
BlaC01, 5 cm	2,0
BlaC01, 28 cm	2,2
GC-191, 25 cm	1,5
GC-191, 218 cm	16,0
GC-191, (core catcher)	8,0
GC-193, 50 cm	15,0
GC-193, 150 cm	1,8
GC-193, 250 cm	26,8

The isotopic composition δ13C(‰,VPDB) of dissolved inorganic carbon in pore waters ranges among all samples between -2,0 and +0,2 ‰, with the reference cores being comfortably within this narrow range (see *Table 13*). The DIC concentrations also show little variation between samples, with the lowest and highest recorded concentrations only being 2 cm apart in the upper part of BlaC03. The reference samples are also within this narrow range between 1,8 and 2,4 mM of DIC.

Table 13. DIC concentration along with its stable carbon isotope anomaly, of porewater extracted of blade cores and multicores at given depths.

		Depth (cm)	**d13C VPDB (‰)**	**DIC (mM)**
Bacterial mat	BlaC01	2	**-0.3**	**1.9**
	BlaC01	6	**-0.1**	**2.1**
	BlaC01	12	**0.2**	**1.9**
Bacterial mat	BlaC03	2	**-0.8**	**1.8**
	BlaC03	4	**-2.0**	**2.4**
	BlaC03	8	**-0.7**	**2.0**
	BlaC03	12	**-1.3**	**2.0**
Reference cores	MC148#5 2	2	**-0.2**	**2.0**
	MC148#5 6	6	**-0.5**	**2.3**
	MC148#5 12	12	**-0.7**	**2.2**

5.4 Sediment core correlation

Three gravity cores were of particular focus in the attempt to correlate stratigraphy, GC-113 collected during HACON-19, and GC-191 and GC-193 from the HACON-21 cruise (see *Figure 15*). Near the surface of the cores, it is hard to reconcile common patterns in the distribution of parameters, therefore horizon zero is only correlated in GC-193 and GC-113, this horizon has a strong MS signal with a relatively long wavelength with a strong or average element signal. Between the horizons zero and one it was hard to reconcile any commonalities, GC-191 have two MS peaks in this interval with fairly strong Fe and Cu, while GC-193 have no particular MS peaks and weak elemental signals, except for one peak in Mn, and similarly to GC-191, GC-113 have two peaks of MS along with stronger elemental signals. Horizons one through nine have largely been chosen based on the MS and *Ln(Fe/Ti)* as corroboration. Horizon three have the second highest MS peak along with a strong XRF signal of Fe and Cu in all three gravity cores. The correlated points 1, 2, 3 and 4 are

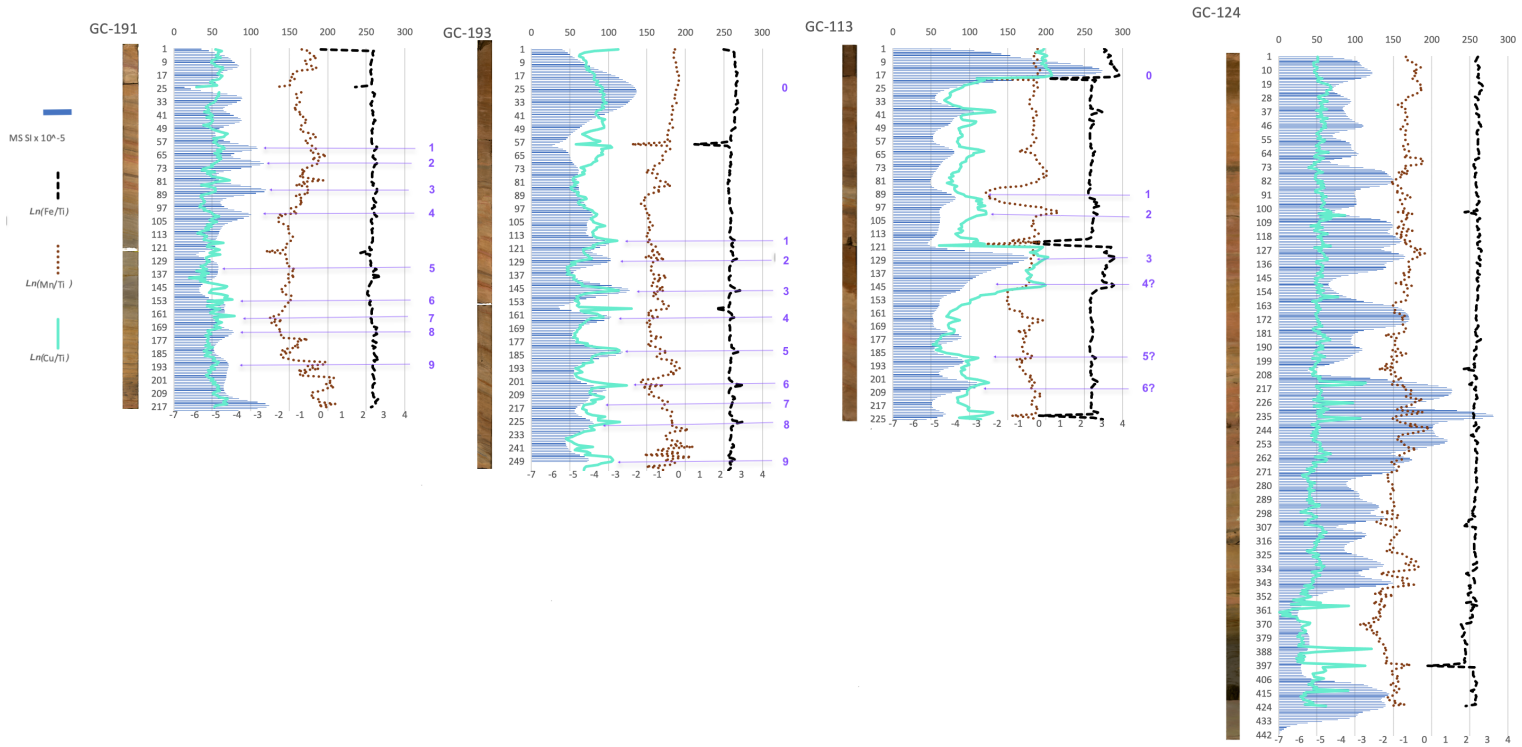

Figure 15. Correlation of gravity cores with MS and XRF of the natural logarithm of the ratio of iron, manganese, and copper against titanium, see the dashed black, pointed brown and solid turquoise lines respectively. GC-124 provide a reference to compare the strength of peaks in MS and elements.

positioned with redder beddings in thicknesses of 2.5, 5, 3.5 and 1.5 cm respectively in GC-191 and GC-191. The correlation points 5 through 9 have relatively weaker MS peaks in GC-191.

6 Discussion

6.1 Sediment biogeochemistry

Ranges of DIC in marine environments are between 0,02 and 5 mM, but the most usual range is between 0,1 and 1mM (Cole & Prairie, 2014) this places the measured DIC concentrations (see *Table 13*) within background levels. Which is also the case for the $\delta^{13}C$(‰,VPDB) range in the DIC of the porewater being close to 0‰. Miocene and Holocene values of marine organic carbon are mostly heavier than -23 ‰, while modern values are mostly lighter than -23 ‰ (Dean et al., 1986). Because of that, it can be assumed the reference site OF MUC-148 represents the background conditions for marine organic carbon of roughly -24 ‰ $\delta^{13}C$. There seems to be some process that preferentially picks up lighter ^{12}C and incorporates it into organic compounds in the surface sediment of both blade cores, with higher intensity nearer to the seafloor surface. The slight increase in the isotopic weight of organic carbon in BlaC01, is somewhat reflected in a small trend of the increased isotopic weight of porewater DIC in BlaC01. Although the first parameter increases with over 5 ‰ from the surface to 12 cm depth, the second increases only 0,5 ‰ over the same interval. This effect is interpreted as produced by chemoautotrophic DIC assimilation by sulfide oxidizing bacteria (fractionation of ~-25‰ from DIC source) (Gilhooly et al., 2007). However, we cannot rule out any contribution from heterotrophic particulate organic carbon fixation which is associated with fractionations of ~-0.6‰.

C/N ratio of BlaC01 and MC-148 are in the normal ratio of C/N for marine organic matter, where ratios of 4 to 10 are typical for marine algae and ratios up to 18 being more typical for mixed marine and terrestrial input (Akinselure, 2022). Beneath 9 cm depth in BlaC03 this ratio is as high as 23,66.

^{15}N is subject to biomagnification in food webs (Won et al., 2018), and the ability to fixate N_2 is only found in prokaryotes (Lengeler, Drews & Schegel, 1999, p.177), leading to these organisms containing the lightest organic nitrogen. It is thus not surprising that the lightest $\delta^{15}N$ of BlaC01 are on the surface where there is a bacterial mat (see *Table 13 & Figure 3*).

In the depths of the open ocean organic nitrogen will typically have $\delta^{15}N$ (‰, N_2^{air}) values between 3 and 5 ‰ (Sigman & Casciotti, 2001, p.1893). In BlaC03 there is clearly more organic carbon in the upper 3 cm (high TOC), with this interval also being quite light in terms of $\delta^{13}C$, this surface interval also contains some the heavier $\delta^{15}N$ values in the core, that are within the range of deep-sea organic nitrogen. Lower down in the core the TON becomes isotopically lighter as the concentrations falls beneath 0,05 % and the C/N ratio increases to a range of 15 to 25. If the lower $\delta^{15}N$ deeper down in BlaC03 in fact are due to N_2 fixation, it could be a response to nitrogen being a limiting nutrient for the microbial community in this site. In MC-148 the range of $\delta^{15}N$ closely matches the concentration of TON, with lower TON translates isotopically lighter TON, and vice versa. This could be indicative of a slight increase in nitrogen fixation when less is available in an area that is distal to the hydrothermal vents.

No evidence for methane oxidation were found in the sediment and DIC geochemistry: the values do not indicate any incorporation of light methane-derived carbon into the bulk sedimentary organic matter nor any inputs to the pore water DIC pool. This is consistent with low methane concentrations.

The dark grey spots in the GC-191 below 200 cm depth strongly suggest bioturbation. That interpretation is supported by seafloor imagery from HACON21 cruise displaying large macrofaunal communities including polychaetas, crustaceans, gastropods, and amphipods around the vent (Ramirez-Llodra et al., 2023).

6.2 Origin of hydrothermal sediments

The direct effect of hydrothermal venting is best observed in the cores collected close to or at the vent field. Material from hydrothermal vents will typically settle in two different fashions. One is the denudation of chimneys and sulfide mounds, resulting in deposits that accumulate along their flanks at short distances in the order of meters or tens of meters. And two is the deposition of oxide particles sinking from a neutrally buoyant plume (Olatunde et al., 2019). In the AVF, the seafloor surface on a vent field is completely dominated by vent deposits due to the relatively lower pelagic contribution to the sediments, as opposed to some other types of vent fields along the AMOR that have significant contributions of glaciogenic sediments (Pedersen et al., 2010).

In hydrothermal vents Cu and Zn precipitate and settle with sulfides more rapidly than Fe (Gartman & Findlay, 2020), which is evident in the blade cores high content of Cu and Zn in the form of chalcopyrite, atacamite, isocubanite and botallackite. Something to note here is the prevalence of the oxidized minerals atacamite and botallackite in the upper 5 cm together, reaching 18% between 1-3 cm depth in BlaC01, but is not registered between 19 and 26 cm. The inverse is observed for the Cu-bearing sulfides constituting 2 to 8 % of the assemblage in the upper 5 cm of BlaC01, while at 25-26 cm chalcopyrite includes 23 % of the assemblage, although at 19-20 cm it is only 1 %, suggesting the interval 25-26 cm contain some particular Cu rich fragments. BlaC03 has the most oxidized Cu minerals in the surface at 4 %, while Fe-Cu sulfides make up 87 % of the minerals at 4-5 cm. Goethite, one of the dominant minerals from the blade cores from AVF is associated as a product of the consumption of iron sulfides by lithotrophic microbes, with pyrrhotite in particular providing better conditions for growth (Toner et al. 2008). This mineral distribution in the blade cores enable us to draw a rough sketch of an environment with Fe and Cu oxyhydroxides covering the seafloor surrounding the vents, with sulfides directly exposed only at or a few meters from the vents, but being replaced by the weathered products of said sulfides as one moves away from the active vents. Sediment compositions seem typical for the black smoker vent mode that occur over 320ºC (Pedersen et al., 2010).

MUC-148 have elemental concentrations in the upper 5 cm that are less heterogenous than those of BlaC01 and BlaC03, but due to the distance from the AFV parts of the sediment will originate from precipitation of hydrothermal plumes.

In the gravity cores the quantitative XRF of selected intervals in conjunction with XRF scans along the whole core have provided evidence for differentiating between lamina based on definitive color change and MS. The markedly redder lamina contains some slightly higher in Fe, Mg and Ca concentrations, while Si, Ti, Al, and Mn are typically higher for the dark grey layers. Many dissolved elements increase in concentration from hydrothermal plumes during lateral dispersal, among these are Fe, Cu, Mn, Ni, PO_4 and SiO_2 (Kleint et al., 2022). Fe is a popular focus for the tracking of hydrothermal plumes in research (German et al., 2016), especially considering its abundance and nice correlation with elevated MS. Concentrations of dissolved Mn in plumes are very sensitive to Mn-oxidizing bacteria, resulting in some plumite deposits being very rich in Mn-bearing bacterial remains (Gartman & Findlay, 2020). In *Figure 15* the red layer containing sample sites B and C (139,5-140,5 cm) in GC-193 have

high Fe, Mn and Cu signals and corresponds with a MS peak, whilst the dark grey layer A (131-132 cm) does not exhibit any elevation for those parameters except for a peak in Mn barely above sites B and C. The quantitative XRF in *Table 1* reflect this by having a higher concentration of Fe and a lower of Mn in both B and C relative to site A. Site F (78-79 cm) in GC-191 on the contrary display relatively elevated signals for both Cu and Mn, but is in the bottom between two MS peaks, and have a relatively normal Fe signal. With the red layer sites D and E (67-68 cm) exhibiting elevated MS, Fe, and normal Cu and Mn signals. Only D show relatively higher concentration of Fe in the quantitative XRF, but E contain the highest Ca as well as high Mg. The red sites have LOI concentrations 2 % higher than the dark grey, which could possibly be attributed to a higher prevalence of carbonate in these mineral assemblages. One last element that indicates higher plume precipitation in the red layers is Ni in *Table 2* where B, C and D all had higher concentrations than the dark gray layers. Red layers also have a higher contrast in the Xray images from GC-191 and GC-193, which can be proof of higher density (Smith et al., 2020). Based on the evidence it seems the redder layers are more characteristic of plumite, while the dark grey represents time intervals with less sedimentation from plumes. Red plumite layers correspond well with peaks in MS and higher density contrast in X-ray-imaging.

6.3 History of vent activity on Aurora Seamount

The gravity cores will be essential to look for cyclicity in plume activity through time as these potentially recorded a far longer time span than the smaller cores. Unfortunately, only one sample from the cores contained sufficient foraminiferal material to be reliably dated (~3 mg foraminiferal material), this was the interval 105-106 cm bsf in GC-193, that yielded a one sigma age range of 27123 to 27344 cal.yr. BP, placing this interval firmly within the glacial period. This value provides an estimated sediment accumulation rate 0,039 mm/yr for GC-193. The stable oxygen isotopic composition of foraminifera along the core can be used to obtain information about the Marine oxygen Isotope Stages (Lowe & Walker, 2014) and improve the chronostratigraphy of the cores. This will be measured in future projects as it was not the focus of this thesis. Among the peaks in MS and elemental signals from XRF scans, all but one is above this date stratigraphically. One process that could complicate this attempt to establish a stratigraphy of the Aurora seamount, is mass wasting. As the Aurora seamount is a volcanic construction as evident by dredge samples and observation of pillow basalts on

the seamount (Michael et al., 2003; Pedersen et al., 2010), one can expect eruptions to produce unstable slope flanks that could be mobilized during or at some point after an eruption. The maximum tilt of layers recorded in GC-193 are around 30º, as the core section were not split along the same vertical plane this is probably the minimum angle of the seabed at time of deposition. It would likely that some of the lithologies observed in the gravity cores are in fact deposited by mass wasting, or that this could have eroded existing material and replaced it. As established in section **7.2**, red layers in the gravity cores can be assumed to be plumite-dominated. Sedimentary layers can appear dark grey for several different reasons, one could be due to sulfides in anoxic environments that absorb more light (Lengeler, Drews, & Schegel, 1999, p.726), however there is no proof this is the case in the gravity cores, rather the relatively higher content of Si, Ti and Al, along with low MS signals could suggest these intervals are the result of periods of lower plumite precipitation. The correlation label "0" in *Figure 15* have the strongest MS signal and a similar color between GC-113 and GC-193, it is more likely the result of mass wasting from the seamount rather than a plumite, as no comparable layer is found close to the surface in GC-191 that is situated further away from the AVF than GC-113 and GC-193. This mass wasting may have removed younger plumite nearer to the surface in GC-193 that otherwise could connect peaks in MS and elements seen in GC-191 and GC-113. Between GC-191 and GC-193 MS peaks occur at intervals with comparable distances. GC-113 contain an interval between 117-145 cm, and correlation labels "3" and "4" with similar color to the assumed mass wasting "0". GC-107 have intense positive MS signal right beneath the present seafloor (*Figure 10),* coupled together with the proximity to GC-193 it provides further evidence of an event localized around the vent field. Thus, if one assumed the accumulation rate extrapolated from the single carbon date to apply down core as well it would likely underestimate the age of the red plumite layers. Assuming the higher estimate for accumulation rate to be correct, the correlation layer 9 would be roughly: 2490mm/0,039mm/yr = 64 000 yr.BP, placing all these correlated layers within the last glacial cycle (Weichselian) (Lowe & Walker, 2014). Correlation layer 1 through 4 appear distinctive of plumites in all three cores. *Table 14* demonstrate the uncertain estimates for age that one single dated sample provide.

Table14. Ages of plumite layers when extrapolated from linear accumulation rate of 0,039.

Plumite layer GC-193	Age with accumulation rate of 0,039mm/yr	approximate thickness of layer mm	Duration of layer with 0,039mm/yr
1	29744	25	641
2	32051	50	1282
3	36923	35	897
4	41282	15	385

GC-116 and GC-118 situated in the rift valley 6,5 and 13,4 km north and south of the AVF respectively, are both probably good candidates to contain records of plume intensity, as the accumulation rate might be even lower and both cores contain long intervals of higher MS signals and intervals of comparably less MS peaks. For GC-116 these intervals are roughly 80-125, 225-320 cm and 410-440 cm, and for GC-118 they are roughly 75-130, 275-325 and below 475 cm bsf. A problem is these cores are all below the lysocline and near or below the local carbonate compensation depth of circa 4000 m (Bradley, 2015), resulting in layers absent of biogenic carbonate that can be dated. The magma supply beneath MORs is responsible for fueling the hydrothermal activity as it brings more partial melt that will become cooled and provide elements for the hydrothermal fluids that are produced. Under most of the crust the mantle is a solid state and can only melt under three different conditions, rise in temperature, lowering of pressure, or change in composition (Winter, 2014). During phases of sinking global temperatures, water in the form of glacial ice have accumulated on the continents, resulting in lower sea level and subsequently relatively lower pressure over MOR (Hasenclever et al., 2017).That hypothesis was first introduced by Lund and Asimow (2011), suggesting a causal relationship between sea level change and mid-ocean ridge magmatism. However, it is still debated, and more studies are needed to evaluate this hypothesis. During the peak of the Last Glacial Maxima (LGM) (23 kyr BP) sea level was at least 120 m lower than that of today (Lowe & Walker, 2014).

Hasenclever et al., (2017) reported results from models that predicted a 60 m relative sea level fall over 15 kyr would cause a 12 % increase in magma production on the global MORs. The

thin crust at the Gakkel ridge especially thin towards the eastern side of the Aurora Seamount, around 1,9-3,3 km (German et al. 2022), this may cause the magma chambers beneath the ridge to be extra susceptible to respond to changes in sea level as it would alleviate some of the pressure provided by the water column. In *Figure 16* are the different responses to glacial isostatic adjustments in the lithosphere at 2,5 km depth during the LGM modeled by Vachon et al., (2022). According to this model the forebulge caused by the Barents and Greenland ice sheets would have caused the crust to be lifted around 10 m relative to current level, which might have contributed to decompression melting at along sector of the ridge and increased vent activity. However, the complex tectonic dynamics of this area hinder an accurate interpretation of the controlling factors for the Aurora vent activity over time. The low sea-level during glacial maxima and deglaciation might have partially contributed to enhanced plumite deposition along the seamount flanks but more accurate geochronology for these cores must be established.

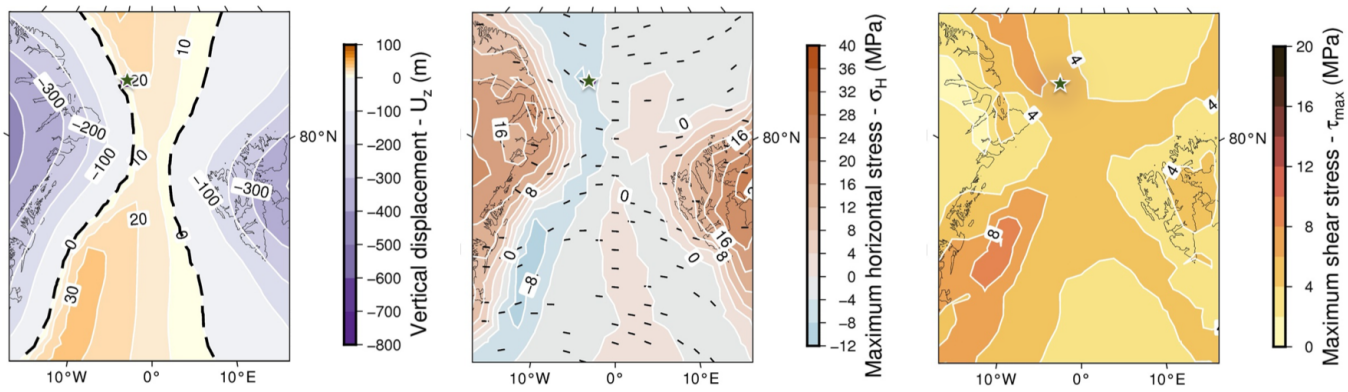

Figure 16. Tectonic conditions modeled for the Fram Strait during the LGM (23 kyr BP), by Vachon et al., (2022). Green star is added to signify the position of the Aurora Seamount.

7 Conclusions

In the generation of new oceanic crust, deep sea hydrothermal vents are focus points for releasing huge amounts of reduced elements into the oceans and act as conduits for the cooling of magma ascending from the mantle. Vents are also the habitat for many unique microorganisms that are sustained entirely by the reductive potential of elements and compounds released by the reaction between hot mantle and seawater. Venting on the Gakkel Ridge was first proven in 2001, and visual confirmation of hydrothermal venting on the Aurora seamount was done in 2014.

The AVF has in the last four years been the target of two cruises that have resulted in new insight into hydrothermal venting in the Arctic Ocean and how it relates to vents worldwide. However, information regarding the temporal evolution of vents is not well constrained yet. In this thesis an attempt was made to characterize the geochemistry and mineralogy of plumites in cores collected from the AVF, the flanks of the seamount and the surrounding Rift Valley and investigate the sedimentary signature of chemoautotrophic microorganisms on the sediments around the AVF. The sediments next to the active vents (BlaC01, BlaC03) are dominated by iron and cupper sulfides and oxyhydroxides representing chimney debris. The plumite in the gravity cores show some enrichment in Fe, Mn and lower carbonate content than the background sediment and non-plumite affected sediment layers, both semi-quantitatively (XRF scans) and quantitatively (XRF %).

One successful carbon dated sample provided evidence for periods of relatively high plume intensity from Aurora before the LGM during the Weichselian. But without dating beneath the plumite layers age estimations become the subject for high degrees of uncertainty. Many gravity cores from the previous HACON19 cruise remains unsplit and will be the subject of future research. The amount of foraminiferal tests for radiocarbon dating did not allow for high resolution geochronology so I suggest using foraminiferal oxygen isotopes (requires ~10 foraminiferal tests) for some better constraint using the Marine Isotope Stages. That would enable us to better constrain the temporal distribution of plumites at the Aurora vent field.

References

Akinselure, A. A. (2022). The Use of Foraminiferal Geochemistry to Investigate Methane Seepage at the Svyatogor Ridge, Arctic Ocean [Master thesis, UiT Norges arktiske universitet]. https://munin.uit.no/handle/10037/25353

Armstrong, H. A., & Brasier, M. D. (2004). Foraminifera. In Microfossils (pp. 142–187). John Wiley & Sons, Ltd. https://doi.org/10.1002/9781118685440.ch15

AvaaTech. (n.d.). XRF core scanner | Avaatech | Analytic Solutions. Avaatech. Retrieved March 10, 2023, from https://www.avaatech.com/xrf-core-scanner/

Beaulieu, S. E., Baker, E. T. and German, C. R. (2015) Where are the undiscovered hydrothermal vents on oceanic spreading ridges?, *Deep Sea Res. Part II Top. Stud. Oceanogr.*, 121, p.202–212, doi:10.1016/j.dsr2.2015.05.001

Beaulieu, S. (2016) *Deep-Sea Vent Discoveries.* National Oceanic and Atmosphere Administration. (retrieved: 17.11.22) https://sos.noaa.gov/catalog/datasets/deep-sea-vent-discoveries/#:~:text=This%20subset%20of%20the%20InterRidge,m%2C%20as%20of%20year%202016.

Beta Analytic (2015, April 14). *AMS Dating Forams and Ostracods.* https://www.radiocarbon.com/calendar-calibration-carbon-dating.htm

Bradley, R.S., (2015) PALEOCLIMATOLOGY Reconstructing Climates of the Quaternary (3rd ed.) Elsvier.

Bunz, S. & Ramirez-Llodra, E. (2019) *RV Kronprins Håkon (cruise no. 2019708) Longyearbyen – Longyearbyen 19.09. – 16.10.2019.* Retrieved from: https://cage.uit.no/cruise/hacon-frinatek-cruise/

Bunz, S. & Ramirez-Llodra, E. (2021) *RV Kronprins Håkon (cruise no. 20211711) Longyearbyen – Longyearbyen 28.09 – 21.10.2021.* Retrieved from: https://cage.uit.no/cruise/hacon-frinatek-cruise-hacon21/

Cole, J. J., & Prairie, Y. T. (2014). Dissolved CO2 in Freshwater Systems☆. In Reference Module in Earth Systems and Environmental Sciences. Elsevier. https://doi.org/10.1016/B978-0-12-409548-9.09399-4

Dean, W. E., Arthur, M. A., & Claypool, G. E. (1986). Depletion of 13C in Cretaceous marine organic matter: Source, diagenetic, or environmental sigal? Marine Geology, 70(1), 119–157. https://doi.org/10.1016/0025-3227(86)90092-7

Engen, Ø., Faleide, J. I., & Dyreng, T. K. (2008). Opening of the Fram Strait gateway: A review of plate tectonic constraints. Tectonophysics, 450(1), 51–69. https://doi.org/10.1016/j.tecto.2008.01.002

Forwick, M., (2013) How to use XRF core scanner data acquired with the Avaatech XRF core scanner at the Department of Geology, University of Tromsø. *A short manual compiled by Matthias Forwick University of Tromsø, Department of Geology, N-9037 Tromsø.* UiT.

Gartman, A., & Findlay, A. J. (2020). Impacts of hydrothermal plume processes on oceanic metal cycles and transport. Nature Geoscience, 13(6), Article 6. https://doi.org/10.1038/s41561-020-0579-0

German, C. R., Bowen, A., Coleman, M. L., Honig, D. L., Huber, J. A., Jakuba, M. V., Kinsey, J. C., Kurz, M. D., Leroy, S., McDermott, J. M., de Lepinay, B. M., Nakamura, K., Seewald, J. S., Smith, J. L., Sylva, S. P., Van Dover, C. L., Whitcomb, L. L. and Yoerger, D. R. (2010) Diverse styles of submarine venting on the ultraslow spreading Mid-Cayman Rise, Proc. *Natl. Acad. Sci., 107(32),* 14020–14025, doi:10.1073/pnas.1009205107, 2010.

German, C. R., Casciotti, K. A., Dutay, J.-C., Heimbürger, L. E., Jenkins, W. J., Measures, C. I., Mills, R. A., Obata, H., Schlitzer, R., Tagliabue, A., Turner, D. R. and Whitby, H. (2016) Hydrothermal impacts on trace element and isotope ocean biogeochemistry, *Philos. Trans. R. Soc. A Math. Phys. Eng. Sci.*, (*374),* no.2081, 20160035, doi:10.1098/rsta.2016.0035, 2016.

German, C. R., Reeves, E. P., Türke, A., Diehl, A., Albers, E., Bach, W., Purser, A., Ramalho, S. P., Suman, S., Mertens, C., Walter, M., Ramirez-Llodra, E., Schlindwein, V., Bünz, S., & Boetius, A. (2022). Volcanically hosted venting with indications of ultramafic influence at Aurora hydrothermal field on Gakkel Ridge. Nature Communications, 13(1), Article 1. https://doi.org/10.1038/s41467-022-34014-0

Geotek Ltd. (n.d.). Multi-Sensor Core Logger (MSCL-S). PRODUCTS. Retrieved March 11, 2023, from https://www.geotek.co.uk/products/mscl-s/

Geotek Ltd. (2016) *Multi-Sensor Core Logger* [Manual] https://www.geotek.co.uk/wp-content/uploads/2016/04/MSCL-manual-1-Nov-16.pdf

Gilhooly, W. P., Carney, R. S., & Macko, S. A. (2007). Relationships between sulfide-oxidizing bacterial mats and their carbon sources in northern Gulf of Mexico cold seeps. Organic Geochemistry, 38(3), 380–393. https://doi.org/10.1016/j.orggeochem.2006.06.005

Goar, C., 2022) *Characterization of benthic foraminiferal ecology and ability to live in fluid emissions in extreme arctic environments* [Master's thesis, Universite de Bretagne Occidentale]

Funder, S, (1982) 14C-dating of samples collected during the 1979 expedition to North Greenland. The Geological Survey of Greenland Report no. 110, p. 9-13.

Hasenclever, J., Knorr, G., Rupke, L.H., Køhler, P, Morgan, J., Garofalo, K,..... Hall, I.R. (2017) Sea level fall during glaciation stabilized atmospheric CO2 by enhanced volcanic degassing. Nature Communications. DOI: 10.1038/ncomms15867

Heaton, T. J., Köhler, P., Butzin, M., Bard, E., Reimer, R. W., Austin, W. E. N., Ramsey, C. B., Grootes, P. M., Hughen, K. A., Kromer, B., Reimer, P. J., Adkins, J., Burke, A., Cook, M.

S., Olsen, J., & Skinner, L. C. (2020). Marine20—The Marine Radiocarbon Age Calibration Curve (0–55,000 cal BP). Radiocarbon, 62(4), 779–820. https://doi.org/10.1017/RDC.2020.68

Håkansson S, (1973) University of Lund Radiocarbon Dates VI. Radiocarbon 15, p. 493-513.

Jakobsson, M., Mayer, L., Coakley, B., Dowdeswell, J. A., Forbes, S., Fridman, B., Hodnesdal, H., Noormets, R., Pedersen, R., Rebesco, M., Schenke, H. W., Zarayskaya, Y., Accettella, D., Armstrong, A., Anderson, R. M., Bienhoff, P., Camerlenghi, A., Church, I., Edwards, M., … Weatherall, P. (2012). The International Bathymetric Chart of the Arctic Ocean (IBCAO) Version 3.0: IBCAO VERSION 3.0. Geophysical Research Letters, 39(12), n/a-n/a. https://doi.org/10.1029/2012GL052219

Klein, F., Grozeva, N.G. & Seewald, J.S. (2019) Abiotic methane synthesis and serpentinization in olivine-hosted fluid inclusions. *PNAS. (vol. 106, no. 36)* p.17666–17672. https://www.pnas.org/cgi/doi/10.1073/pnas.1907871116

Klotz, Bryant, D.A. & Hanson, T.E. (2011) The microbial sulfur cycle. Frontiers in Microbiology. (Vol.2, no.241) p.1-2

Korff, S. A. (1940). On the contribution to the ionization at sea-level produced by the neutrons in the cosmic radiation. Journal of the Franklin Institute, 230(6), p.777–779. https://doi.org/10.1016/S0016-0032(40)90838-9

Lengeler, J.W., Drews, G. & Schegel, H.G. (1999). Biology of the Prokaryotes. Stuttgart: Thieme.

Lund, D. C., & Asimow, P. D. (2011). Does sea level influence mid-ocean ridge magmatism on Milankovitch timescales?: SEA LEVEL AND MID-OCEAN RIDGE MAGMATISM. Geochemistry, Geophysics, Geosystems, 12(12), n/a-n/a. https://doi.org/10.1029/2011GC003693

Mangerud, J and Gulliksen, S, (1975) Apparent radiocarbon ages of Recent marine shells from Norway. Spitsbergen, and Arctic Canada. Quaternary Research 5, p.263-273.

McCollom, T.M. & Shock, E.L. (1997) Geochemical constraints on chemolithoautotrophic metabolism by microorganisms in seafloor hydrothermal systems. *Geochimicaet CosmochimicaActa (61)*, No. 20 p. 4375-4391

Michael, P. J., Langmuir, C. H., Dick, H. J. B., Snow, J. E., Goldstein, S. L., Graham, D. W., Lehnert, K., Kurras, G., Jokat, W., Mühe, R., & Edmonds, H. N. (2003). Magmatic and amagmatic seafloor generation at the ultraslow-spreading Gakkel ridge, Arctic Ocean. Nature, 423(6943), Article 6943. https://doi.org/10.1038/nature01704

Molari, M., Hassenrueck, C., Laso-Perez, R., Wegener, G., Offre, P., Scilipoti, S. & Boetius, A. (2022) Hydrogenotrophic bacteria of Arctic hydrothermal vent plumes belong to a novel cosmopolitan branch of aerobic deep-sea Sulfurimonas. Nat. Microbiol. https://doi.org/10.21203/rs.3.rs-1386537/v1

NOAA. (2023, April 5). [Webdata]. https://gml.noaa.gov/webdata/ccgg/trends/ch4/ch4_annmean_gl.txt

Norwegian Institute for Water Research, Ramirez-Llodra, E., Argentino, C., Baker, M., Boetius, A., Costa, C., Dahle, H., Denny, E., Dessandier, P.-A., Eilertsen, M., Ferre, B., German, C., Hand, K., Hilário, A., Hislop, L., Jamieson, J., Kalnitchenko, D., Mall, A., Panieri, G., … Buenz, S. (2023). Hot Vents Beneath an Icy Ocean: The Aurora Vent Field, Gakkel Ridge, Revealed. Oceanography, 36(1). https://doi.org/10.5670/oceanog.2023.103

Nystuen, J.P. (2007) Jorda skifter ansikt: geologiske prosesser. In K. Rangnes (Ed.), *Landet blir til: Norges geolog* (p. 24-29). Norsk geologisk forening (NGF).

Lasabuda, A. P. E., Johansen, N. S., Laberg, J. S., Faleide, J. I., Senger, K., Rydningen, T. A., Patton, H., Knutsen, S.-M., & Hanssen, A. (2021). Cenozoic uplift and erosion of the Norwegian Barents Shelf – A review. Earth-Science Reviews, 217, 103609. https://doi.org/10.1016/j.earscirev.2021.103609

Olatunde, P.S., Paul, U.J., Thompson, A.A., Edward, A.A., Adjare, L.I., Olaiwola, A.F. & Osiuare E.J. (2019) Hydrothermal Components in Marine Sediments: An Insight into Sea Floor Mineralization Process. *Academic Journal of Chemistry (volume 4, issue 6)* p.27-33

Pedersen, R.B., Thorseth, I.H., Nygård, T.E., Lilley, M.D. & Kelley, D.S (2010) Hydrothermal Activity at the Arctic Mid-Ocean Ridges. *Geophysical Monograph Series 188* p.67-89

Pendleton, R. L., & Nickerson, D. (1951). SOIL COLORS AND SPECIAL MUNSELL SOIL COLOR CHARTS. Soil Science, 71(1), 35.

Ross, P.-S., & Bourke, A. (2017). High-resolution gamma ray attenuation density measurements on mining exploration drill cores, including cut cores. Journal of Applied Geophysics, 136, 262–268. https://doi.org/10.1016/j.jappgeo.2016.11.012
Sievert, S.M., Hugler, M., Taylor, C.D. & Wirsen, C.O. (2008) Chapter 19 Sulfur Oxidation at Deep-Sea Hydrothermal Vents Microbial Sulfur Metabolism. p.238-258 Springer-Verlag Berlin Heidelberg New York

Sigman, D. M., & Casciotti, K. L. (2001). Nitrogen Isotopes in the Ocean. In Encyclopedia of Ocean Sciences (pp. 1884–1894). Elsevier. https://doi.org/10.1006/rwos.2001.0172

Smith, N. T., Shreeve, J., & Kuras, O. (2020). Multi-sensor core logging (MSCL) and X-ray computed tomography imaging of borehole core to aid 3D geological modelling of poorly exposed unconsolidated superficial sediments underlying complex industrial sites: An example from Sellafield nuclear site, UK. Journal of Applied Geophysics, 178, 104084. https://doi.org/10.1016/j.jappgeo.2020.104084

Toner, B.M., Santelli, C.M., Marcus, M.A., Wirth, R., Chan, C.S., McCollom, T., Bach, W. & Edwards., K.J. (2008) Biogenic iron oxyhydroxide formation at mid-ocean ridge

hydrothermal vents: Juan de Fuca Ridge. Geochimica et Cosmochimica Acta Volume (73), Issue 2 p.388-403 https://doi.org/10.1016/j.gca.2008.09.035

Vachon, R., Schmidt, P., Lund, B., Plaza-Faverola, A., Patton, H., & Hubbard, A. (2022). Glacially Induced Stress Across the Arctic From the Eemian Interglacial to the Present—Implications for Faulting and Methane Seepage. Journal of Geophysical Research: Solid Earth, 127(7), e2022JB024272. https://doi.org/10.1029/2022JB024272

Lowe, J. & Walker, M., (2014). Reconstructing Quaternary Environments (3rd ed.). Routledge. https://doi.org/10.4324/9781315797496

Webb, P. (n.d.). 6.3 Density. Retrieved May 14, 2023, from https://rwu.pressbooks.pub/webboceanography/chapter/6-3-density/
Weiss, M. C., Sousa, F. L., Mrnjavac, N., Neukirchen, S., Roettger, M., Nelson-Sathi, S., & Martin, W. F. (2016). The physiology and habitat of the last universal common ancestor. Nature Microbiology, 1(9), Article 9. https://doi.org/10.1038/nmicrobiol.2016.116

Whiticar, M.J., (1999) Carbon and hydrogen isotope systematics of bacterial formation and oxidation of methane. Chemical Geology, 161, p.291-314

Winter, J.D., (2014) Principles of Igneous and Metamorphic Petrology (2nd ed.) Pearson Education Limited

Won, E.J., Choi, B., Hong, S., Khim, J.S. & Shin, K.H., (2018) Importance of accurate trophic level determination by nitrogen isotope of amino acids for trophic magnification studies: A review. Environmental Pollution, 238, p.677-690. https://doi.org/10.1016/j.envpol.2018.03.045.

Yoshino, T., & Katsura, T. (2013). Electrical Conductivity of Mantle Minerals: Role of Water in Conductivity Anomalies. Annual Review of Earth and Planetary Sciences, 41(1), 605–628. https://doi.org/10.1146/annurev-earth-050212-124022